Article

STAT5 and STAT3 balance shapes dendritic cell function and tumour immunity

https://doi.org/10.1038/s41586-025-09000-3

Received: 21 January 2024

Accepted: 9 April 2025

Published online: 14 May 2025

Open access

Check for updates

Jiajia Zhou[1,2], Kole Tison[1,2,3,4], Haibin Zhou[5], Longchuan Bai[5], Ranjan Kumar Acharyya[5], Donna McEachern[5], Hoda Metwally[5], Yu Wang[5], Michael Pitter[1,2], Jae Eun Choi[6,7], Linda Vatan[1,2], Peng Liao[1,2], Jiali Yu[1,2], Heng Lin[1,2], Long Jiang[2,4], Shuang Wei[1,2], Xue Gao[1,2], Sara Grove[1,2], Abhijit Parolia[6,7], Marcin Cieslik[4,6,7], Ilona Kryczek[1,2], Michael D. Green[2,8], Jian-Xin Lin[9], Arul M. Chinnaiyan[6,7,10,11,12], Warren J. Leonard[9], Shaomeng Wang[5,7,11,13,14] ✉ & Weiping Zou[1,2,3,6,11,12] ✉

Immune checkpoint blockade (ICB) has transformed cancer therapy[1,2]. The efficacy of immunotherapy depends on dendritic cell-mediated tumour antigen presentation, T cell priming and activation[3,4]. However, the relationship between the key transcription factors in dendritic cells and ICB efficacy remains unknown. Here we found that ICB reprograms the interplay between the STAT3 and STAT5 transcriptional pathways in dendritic cells, thereby activating T cell immunity and enabling ICB efficacy. Mechanistically, STAT3 restrained the JAK2 and STAT5 transcriptional pathway, determining the fate of dendritic cell function. As STAT3 is often activated in the tumour microenvironment[5], we developed two distinct PROTAC (proteolysis-targeting chimera) degraders of STAT3, SD-36 and SD-2301. STAT3 degraders effectively degraded STAT3 in dendritic cells and reprogrammed the dendritic cell–transcriptional network towards immunogenicity. Furthermore, STAT3 degrader monotherapy was efficacious in treatment of advanced tumours and ICB-resistant tumours without toxicity in mice. Thus, the crosstalk between STAT3 and STAT5 transcriptional pathways determines the dendritic cell phenotype in the tumour microenvironment and STAT3 degraders hold promise for cancer immunotherapy.

Immunotherapy, including ICB and T cell therapy, uses the immune system to eliminate cancer cells[1,2,6]. However, most patients are either poorly responsive to ICB or develop therapeutic resistance. Emerging evidence suggests that ICB does not trigger potent immune responses in patients with limited and impaired dendritic cells[3] (DCs) in the tumour microenvironment (TME). DCs present tumour antigens to prime and activate T cells, thereby driving anti-tumour immunity[4,7–11]. In line with this, increased type 1 dendritic cell (DC1) infiltration correlates with prolonged survival in patients with cancers[12–14]. However, the TME can impede DC1 maturation and function, partly owing to disruptive environmental signals[4,15–17]. Thus, understanding how the DC phenotype is shaped in the TME and exploring strategies to enhance DC1 function are crucial for developing more effective cancer immunotherapy.

Alterations in STAT signalling pathways exert profound effects on anti-tumour responses in the TME[18]. For example, STAT3 is often activated and mediates immune inhibition in the TME[5,19]. STAT3 activation leads to the production of various pro-tumour factors, including VEGF and IL-6, impeding DC maturation and function[20,21]. Moreover, STAT3 signalling can inhibit T helper 1 (T_H1)-type chemokine expression and subdue DC tumour trafficking, resulting in the exclusion of T cells from the TME[21]. By contrast, STAT5 is activated in response to cytokine signals, such as GM-CSF and IL-2[22], and has a positive role in the anti-tumour immune response[23,24]. On this basis, we hypothesized that the balance between the STAT5 and STAT3 transcriptional pathways in DCs may shape the fate of distinct immune responses in the TME, determining ICB responses in patients with cancer.

In this study, we analysed single-cell and bulk RNA-sequencing (RNA-seq) datasets from tumour tissues in patients with cancer who were receiving ICB. We found that the transcriptional pathways of STAT5 and STAT3 in DC1s correlated with T cell immunity and was associated with clinical outcome in patients treated with ICB. Moreover, genetic deletion and pharmacologic inhibition of STAT3 signalling led to DC1 activation and profound anti-tumour T cell immune responses. Furthermore, we provide proof of concept that pharmacological degradation of STAT3 can treat multiple tumour types as monotherapy and sensitize tumours to ICB.

[1]Department of Surgery, University of Michigan Medical School, Ann Arbor, MI, USA. [2]Center of Excellence for Cancer Immunology and Immunotherapy, University of Michigan Rogel Cancer Center, Ann Arbor, MI, USA. [3]Graduate Program in Immunology, University of Michigan, Ann Arbor, MI, USA. [4]Department of Computational Medicine and Bioinformatics, University of Michigan Medical School, Ann Arbor, MI, USA. [5]Division of Hematology and Oncology, Department of Internal Medicine, University of Michigan Medical School, Ann Arbor, MI, USA. [6]Department of Pathology, University of Michigan Medical School, Ann Arbor, MI, USA. [7]Michigan Center for Translational Pathology, University of Michigan Medical School, Ann Arbor, MI, USA. [8]Department of Radiation Oncology, University of Michigan Medical School, Ann Arbor, MI, USA. [9]Laboratory of Molecular Immunology and the Immunology Center, National Heart, Lung and Blood Institute, National Institutes of Health, Bethesda, MD, USA. [10]Howard Hughes Medical Institute, University of Michigan Medical School, Ann Arbor, MI, USA. [11]University of Michigan Rogel Cancer Center, University of Michigan, Ann Arbor, MI, USA. [12]Graduate Program in Cancer Biology, University of Michigan, Ann Arbor, MI, USA. [13]Department of Pharmacology, University of Michigan Medical School, Ann Arbor, MI, USA. [14]Department of Medicinal Chemistry, College of Pharmacy, University of Michigan, Ann Arbor, MI, USA. ✉e-mail: shaomeng@umich.edu; wzou@umich.edu

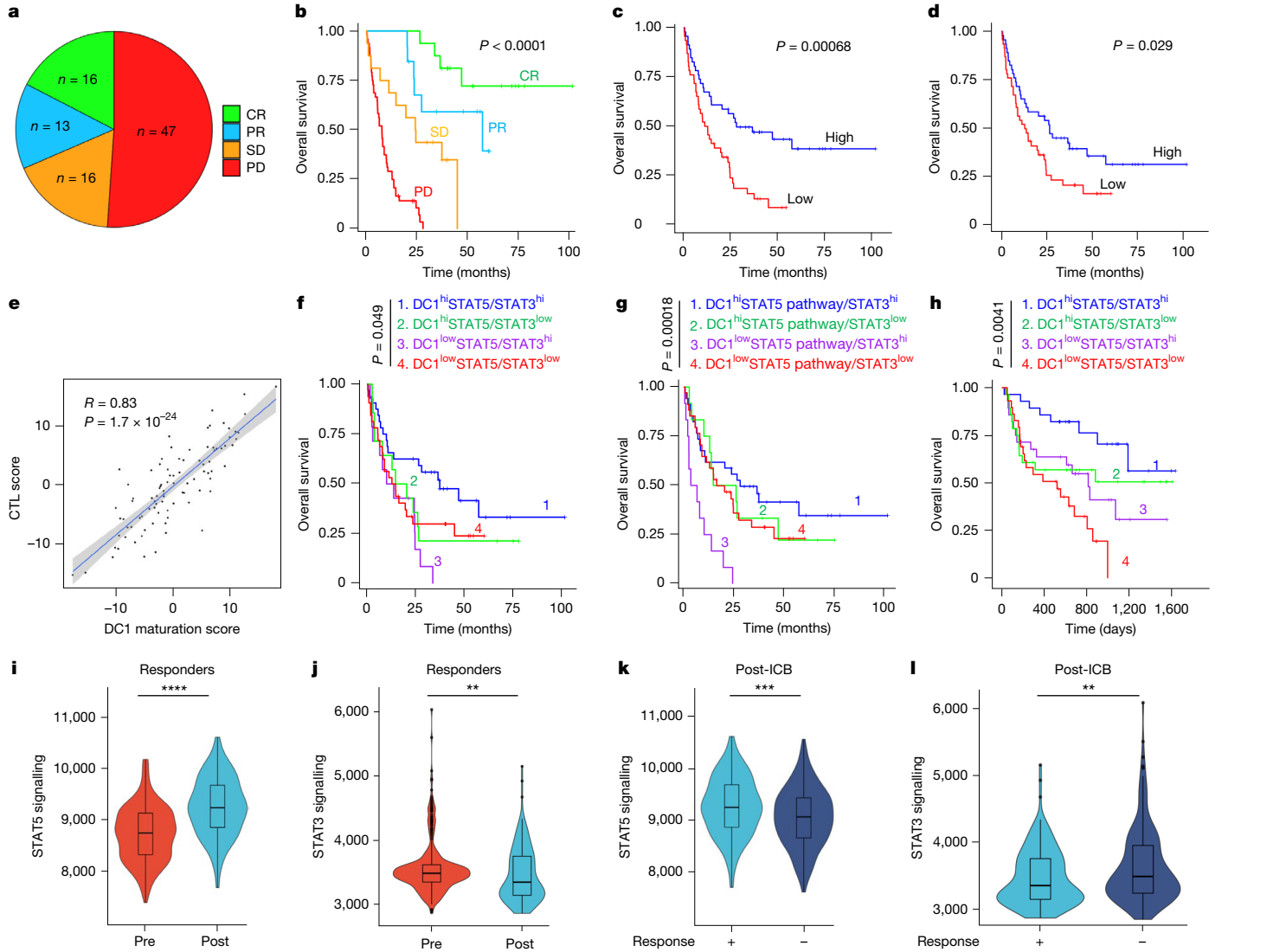

Fig. 1 | Role of DC STAT5 and STAT3 in ICB. a–d, DC1 score and overall survival. **a**, Pie chart of number and percentages show RECIST-defined responses to ICB in cohort 1. CR, complete response; PD, progressive disease; PR, partial response; SD, stable disease. **b–d**, Kaplan–Meier survival curves were stratified by clinical response groups (**b**), cytotoxic T lymphocyte (CTL) score (**c**) and median DC1 maturation score (**d**). $n = 92$; log-rank test. **e**, Pearson correlation analysis shows a correction between CTL score and DC1 maturation score. The shaded area represents the 95% confidence interval. $n = 92$. **f,g**, Kaplan–Meier curves of overall survival in patients from cohort 1 were stratified by DC score and *STAT5*/*STAT3* expression (**f**) or STAT5 transcriptional pathway/*STAT3* expression (**g**). $n = 92$; $P = 0.049$ (**f**) and $P = 0.00018$ (**g**), log-rank test. **h**, Kaplan–Meier curves of overall survival in cohort 2 were stratified by DC score and the ratio of *STAT5* versus *STAT3*. $n = 114$; $P = 0.0041$, log-rank test. **i–l**, STAT5 and STAT3 signalling signatures in DCs in cohort 3. **i,j**, STAT5 (**i**) and STAT3 (**j**) gene signatures in DCs were analysed in post-ICB samples of responders and the respective pre-ICB samples. **k,l**, STAT5 (**k**) and STAT3 (**l**) gene signatures within DCs were compared between non-responders and responders. In box plots, the central line represents the median, the box extends from the 25th to 75th percentiles, and whiskers span the smallest and largest values within 1.5× the interquartile range. Outliers are shown as individual points. Responders: pre- (332 DCs) and post- (170 DCs) treatment (4 patients). Non-responders: pre- (215 DCs), post- (194 DCs) treatment (6 patients). $^{**}P = 0.0012$ (**j**), $^{***}P = 0.00092$ (**k**), $^{**}P = 0.0045$ (**l**) and $^{****}P < 0.0001$ (**i**), Wilcoxon rank-sum test. *P* values are two-sided without correction for multiple comparisons.

Role of DC STAT5 and STAT3 in ICB

The STAT5 and STAT3 transcriptional pathways regulate tumour immune responses[21,23,24]. We thus reasoned that interplay between these two transcriptional pathways in immune cells, particularly in DCs, influences ICB responses in patients with cancer. To examine this possibility, we analysed RNA-seq data from tumour tissues collected before ICB treatment in a patient cohort (cohort 1) at the University of Michigan[25] (Extended Data Table 1). As previously reported[25], among these patients, 17% achieved a complete response to ICB, whereas 14% achieved partial response, 17% had stable disease and 51% had progressive disease according to RECIST (response evaluation criteria in solid tumours) criteria (Fig. 1a), and the complete response group exhibited the longest overall survival rate in cohort 1 (Fig. 1b). To determine whether the clinical response is associated with the effector T cell-mediated anti-tumour response, we evaluated outcomes stratified by expression of T effector cell signatures[26]. Patients with a high $CD8^+$ effector T cell score exhibited improved overall survival (Fig. 1c). Furthermore, we calculated a DC1 maturation score[27]. We found that patients with a high DC1 maturation and function score demonstrated improvements in overall survival resembling those in patients with a high $CD8^+$ effector T cell score (Fig. 1d). This similarity in survival was mirrored by a strong positive correlation between $CD8^+$ effector T cell and DC1 maturation scores (Fig. 1e). Thus, DC-mediated antigen cross-presentation and T cell activation may drive ICB response in patients with cancer.

To explore the role of the relationship between the STAT5 and STAT3 transcriptional pathways in the context of DC1 maturation and function, we stratified patients (cohort 1) by the median DC1 maturation score and the median ratio of *STAT5*/*STAT3* expression into four groups: $DC1^{hi}STAT5/STAT3^{hi}$, $DC1^{hi}STAT5/STAT3^{low}$, $DC1^{low}STAT5/STAT3^{hi}$, and $DC1^{low}STAT5/STAT3^{low}$. Among the four patient groups, those classified as $DC1^{hi}STAT5/STAT3^{hi}$ had the longest overall survival, whereas the other groups exhibited similar survival trends to each other (Fig. 1f). We observed similar results when we stratified patients by the median ratio of STAT5 transcriptional pathway activation and *STAT3* expression (Fig. 1g) and by excluding patients with tumours that were inherently unresponsive to ICB (Extended Data Fig. 1a). We analysed additional patients with melanoma[28,29] (cohort 2), a type of cancer that is sensitive to anti-PD-1 and anti-CTLA-4 therapy (Extended Data Table 2). $DC1^{hi}STAT5/STAT3^{hi}$ in cohort 2 exhibited the longest overall survival, whereas the $DC1^{low}STAT5/STAT3^{low}$ patients had the shortest (Fig. 1h and Extended Data Fig. 1b,c). Thus, the relationship between DC1 maturation and the STAT5 and STAT3 transcriptional pathways may affect responsiveness to ICB.

To solidify this finding, we analysed a single-cell RNA-sequencing (scRNA-seq) dataset from patients with triple-negative breast cancer (TNBC) (cohort 3), and examined DCs in tumour tissues collected before and after ICB treatment[30]. We conducted an analysis of the STAT5 and STAT3 transcriptional pathways in DC clusters. The analysis revealed a bimodal distribution of the STAT3 transcriptional pathway, with the second mode exhibiting a relatively high STAT3 signalling activity (Extended Data Fig. 1d). We conducted a detailed analysis of the STAT5 and STAT3 transcriptional pathways in DC clusters with relatively high STAT3 expression. Of note, STAT5 transcriptional signalling increased in post-ICB samples compared with pre-ICB samples among responders to ICB (Fig. 1i), but such an increase was not observed in non-responders (Extended Data Fig. 1e). Conversely, STAT3 transcriptional signalling showed a decrease in post-ICB samples of responders compared with their pre-ICB samples (Fig. 1j), with no significant change observed in non-responders (Extended Data Fig. 1f). Furthermore, post-ICB samples showed an increase in STAT5 transcriptional signalling and a reduction in STAT3 transcriptional signalling in responders relative to non-responders (Fig. 1k,l). We then examined the STAT5 and STAT3 transcriptional signalling pathways in specific DC subsets in these patients[30] (cohort 3). Using the Louvain algorithm for shared nearest neighbours clustering and uniform manifold approximation and projection (UMAP) visualization to distinguish the cells, we conducted an analysis with two major distinct DC clusters, conventional DCs (cDCs) and monocyte-derived DCs (moDCs) (Extended Data Fig. 1g). In the cDC subset, the post-ICB samples from responders displayed increased STAT5 transcriptional signalling and decreased STAT3 transcriptional signalling compared with pre-ICB samples (Extended Data Fig. 1h,i). These changes were not discernible in the non-responder group (Extended Data Fig. 1j,k). In moDCs, an increase in STAT5 signalling was observed in the post-ICB samples from responders, whereas STAT3 transcriptional signalling remained unchanged compared with pre-ICB samples in both responders and non-responders (Extended Data Fig. 1l–o). Furthermore, in the post-ICB samples, we observed a noticeable increase in STAT5 transcriptional signalling and a corresponding decrease in STAT3 transcriptional signalling in the responders compared to the non-responders within cDCs (Extended Data Fig. 1p,q). In moDCs, neither STAT5 nor STAT3 transcriptional signalling showed significant differences between post-ICB samples from responders and non-responders (Extended Data Fig. 1r,s). Collectively, ICB treatment dynamically reprograms the STAT5 and STAT3 transcriptional signalling pathways in cDCs, affecting ICB efficacy.

STAT3 restrains STAT5-driven DC function

Given the negative effect of STAT3 transcriptional activity on DC maturation and ICB response, we examined whether alteration of STAT3 activity would affect DC phenotype. We used short hairpin RNAs (shRNAs) targeting *Stat3* (sh*Stat3*) in JAWSII cells, a DC line[31,32] (Fig. 2a). Knocking down STAT3 expression resulted in a robust increase in phosphorylation of STAT5 (pSTAT5) and a minor increase in pSTAT1, but had no effect on pSTAT6 and p-p65 in JAWSII cells cultured with GM-CSF (Fig. 2a). We crossed $Stat3^{fl/fl}$ mice with $Xcr1^{cre}$ mice (which express mCherry under the control of the *Xcr1* promoter) and generated cDC1-specific STAT3 knockout ($Stat3^{-/-}$) mice. We used $Stat3^{fl/fl}Xcr1^{+/+}$ mice as the $Stat3^{+/+}$ controls, enabling us to use mCherry fluorescence to validate knockout specificity in the mouse offspring (Extended Data Fig. 2a). No mCherry expression was detected in other immune cells in $Stat3^{-/-}$ mice (Extended Data Fig. 2b). We confirmed the absence of STAT3 protein in cDC1s generated from $Stat3^{-/-}$ mice (Fig. 2b and Extended Data Fig. 2c). At 6 to 10 weeks of age, $Stat3^{+/+}$ and $Stat3^{-/-}$ mice exhibited similar body size (Extended Data Fig. 2d), similar appearance of lymphoid organs (Extended Data Fig. 2e) and equivalent levels of $CD8^+$ and $CD4^+$ T cells in tissues (Extended Data Fig. 2f,g). Notably, we detected an increase in STAT5 activation in $Stat3^{-/-}$ cDC1s compared with $Stat3^{+/+}$ cDC1s (Fig. 2b). An unbiased phospho-receptor kinase array showed higher levels of pSTAT5 in $Stat3^{-/-}$ cDC1s than $Stat3^{+/+}$ cDC1s (Fig. 2c). Thus, STAT3 restrains STAT5 activation in DCs. Flow cytometry analysis revealed higher levels of typical DC maturation markers, including major histocompatibility complex class I (MHCI; Fig. 2d), major histocompatibility complex class II (MHCII; Fig. 2e), CD80 (Fig. 2f and Extended Data Fig. 2h) and CD86 (Fig. 2g and Extended Data Fig. 2h) in $Stat3^{-/-}$ cDC1s than in $Stat3^{+/+}$ cDC1s.

To explore how STAT5 activation is regulated in DCs, we assessed the expression profile of a range of cytokine receptors that are capable of activating STAT5, including the receptors for IL-2, IL-3, IL-5, IL-7, IL-15, IL-21 and GM-CSF, in cDC1s. Among these cytokine receptors, we detected higher transcript levels of GM-CSF receptors, *Gmrα* (also known as *Csf2ra*) and *Gmrβ* (also known as *Csf2rb*), compared with other cytokine receptors in cDC1s (Extended Data Fig. 2i). Knocking down GMRβ with specific shRNAs resulted in a decrease in phosphorylation of JAK2, STAT5 and STAT3 (Fig. 2h), but not of JAK1, TYK2, JAK3 and STAT1 in JAWSII cells cultured with GM-CSF (Extended Data Fig. 2j). Moreover, knocking down JAK2 caused a profound reduction of pSTAT5 and a moderate reduction of pSTAT3, but not pSTAT1, in JAWSII cells in response to GM-CSF (Fig. 2i). GM-CSF stimulation induced the phosphorylation of JAK2, but not JAK1, JAK3 or TYK2 in JAWSII cells (Extended Data Fig. 2k). Similar findings have been reported in human neutrophils[33]. Thus, GM-CSF and signalling pathways downstream of the GM-CSF receptor may regulate STAT5 activation via JAK2 in DCs.

We next investigated whether STAT3 is involved in the GMR–JAK2–STAT5 axis in DCs. We found that $Stat3^{-/-}$ and $Stat3^{+/+}$ cDC1s expressed similar levels of GM-CSF (Extended Data Fig. 2l) and GMRβ (Extended Data Fig. 2m). Then, we performed a reciprocal co-immunoprecipitation assay with anti-GMRβ and anti-JAK2 in $Stat3^{-/-}$ and $Stat3^{+/+}$ cDC1s. Co-immunoprecipitation experiments demonstrated the co-existence of GMRβ, JAK2 and STAT5 in activated cDC1s (Fig. 2j,k). Despite similar levels of GMRβ and JAK2 in the co-immunoprecipitation products of $Stat3^{-/-}$ and $Stat3^{+/+}$ cDC1s (Fig. 2j,k), genetic deletion of STAT3 led to an increase in the interaction between GMRβ and STAT5 (Fig. 2j) and between JAK2 and STAT5 (Fig. 2k). sh*Stat3* JAWSII cells (Fig. 2a) and $Stat3^{-/-}$ cDC1s (Fig. 2b) expressed higher levels of pSTAT5 than their counterparts. The data suggest that STAT3 may restrain the GMRβ–JAK2–STAT5 signalling pathway, thereby affecting DC phenotype and function in vitro (Fig. 2d–g and Extended Data Fig. 2h). Given that increased IL-6 and activated STAT3 are often observed in the TME, we assessed the expression of IL-6 and its receptors in human and mouse DCs. IL-6-expressing DCs represented a negligible fraction among IL-6-positive cells from patients with TNBC[30] (cohort 3) (Extended Data Fig. 2n). Mouse $Stat3^{+/+}$ and $Stat3^{-/-}$ cDC1s expressed low levels of IL-6 (Extended Data Fig. 2o,p). Moreover, cDC1s expressed similar amounts of IL-6 receptor transcripts (*Il6ra* and *Il6st*) (Extended Data Fig. 2q,r)

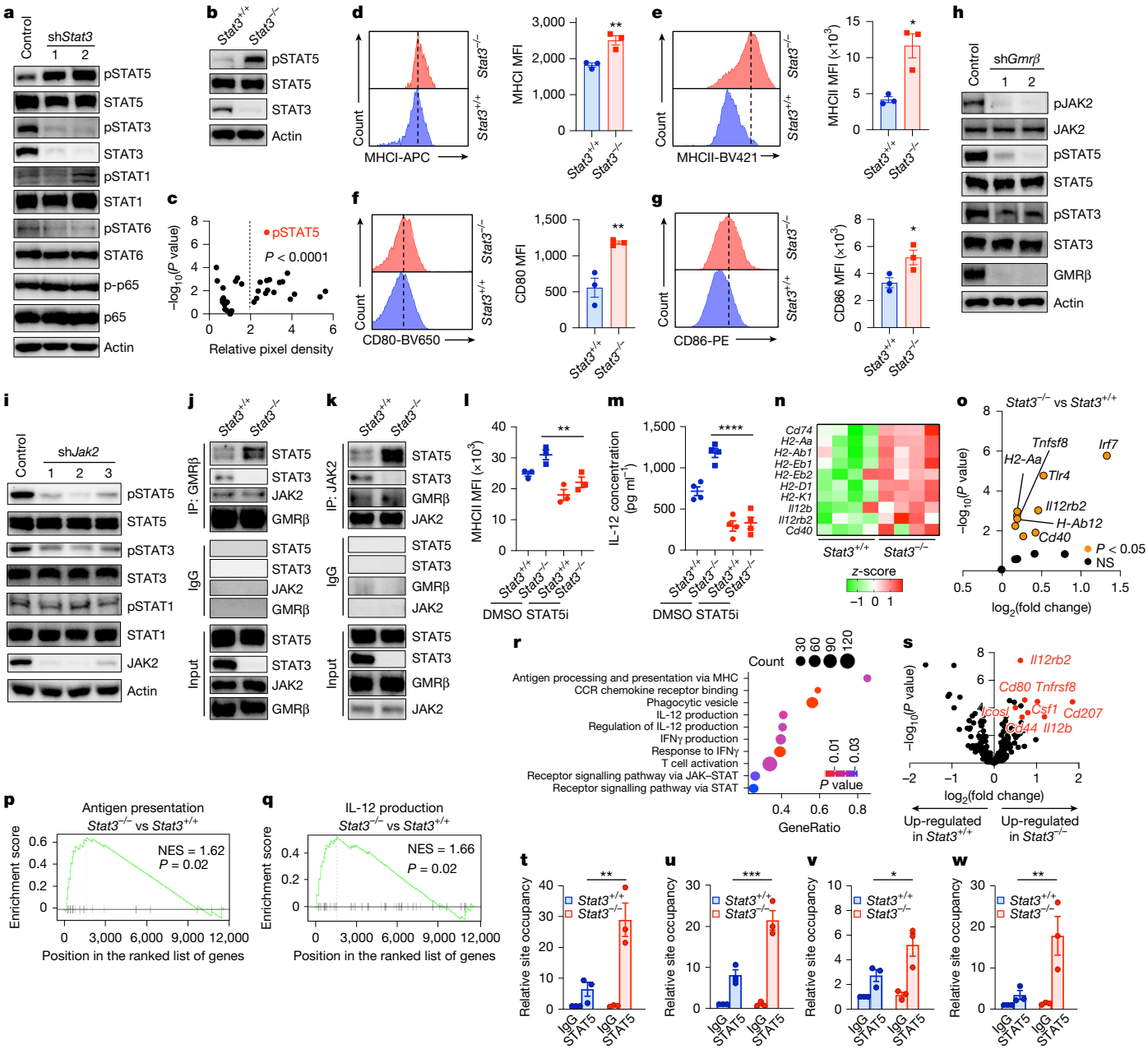

Fig. 2 | STAT3 restrains STAT5-driven DC function. a,**b**, Immunoblots of transcription factors in sh*Stat3*JAWSII cells (**a**) and *Stat3*$^{+/+}$ and *Stat3*$^{-/-}$ cDC1s (**b**). $n = 3$. **c**, Scatter plots of relative pixel density versus corresponding $-\log_{10}$ (*P* value) for a phospho-antibody array incubated with lysate from LPS-stimulated *Stat3*$^{+/+}$ and *Stat3*$^{-/-}$ cDC1s. $n = 4$. **d**,**e**, Fluorescence-activated cell sorting (FACS; left) and mean fluorescence intensity (MFI; right) of MHCI (**d**) and MHCII (**e**) in *Stat3*$^{+/+}$ and *Stat3*$^{-/-}$ cDC1s. Data are mean ± s.e.m., $n = 3$; $^{**}P = 0.0084$ (**d**) and $^{*}P = 0.0125$ (**e**), unpaired two-tailed *t*-test. **f**,**g**, FACS and MFI of CD80 (**f**) and CD86 (**g**) in *Stat3*$^{+/+}$ or *Stat3*$^{-/-}$ cDC1s. Data are mean ± s.e.m., $n = 3$; $^{**}P = 0.0098$ (**f**) and $^{*}P = 0.0453$ (**g**), unpaired two-tailed *t*-test. **h**,**i**, Immunoblots of transcription factors in JAWSII cells cultured with GM-CSF and transfected with sh*Gmrβ* (**h**) or sh*Jak2* (**i**). $n = 3$. **j**,**k**, Immunoprecipitation with anti-GMRβ (**j**) or anti-JAK2 (**k**) shows the interaction between GMRβ and transcription factors in activated *Stat3*$^{+/+}$ and *Stat3*$^{-/-}$ cDC1s. $n = 2$. **l**,**m**, FACS analysis of MHCII (**l**) and IL-12 enzyme-linked immunosorbent assay (ELISA; **m**) in *Stat3*$^{+/+}$ and *Stat3*$^{-/-}$ cDC1s cultured with STAT5i. Data are mean ± s.e.m., $n = 3$, $^{**}P = 0.0079$ (**l**); $n = 4$, $^{****}P < 0.0001$ (**m**); one-way ANOVA. **n**–**q**, Heat map comparing expression of DC maturation genes in *Stat3*$^{+/+}$ versus *Stat3*$^{-/-}$ cDC1s as *z*-scores (**n**) or calculated with EdgeR (**o**), and GSEA shows differences in expression of genes associated with antigen processing and presentation (**p**) and IL-12 production (**q**). NES, normalized enrichment score. **r**,**s**, RNA-seq analysis of LPS-stimulated *Stat3*$^{+/+}$ and *Stat3*$^{-/-}$ cDC1s shows changes in genes associated with multiple signalling pathways (**r**) and STAT5 signalling (**s**). **t**–**w**, ChIP–qPCR shows promoter occupancy of *H2-D1* (**t**), *H2-Eb1* (**u**), *Cd80* (**v**) and *Cd86* (**w**) in LPS-treated *Stat3*$^{+/+}$ or *Stat3*$^{-/-}$ cDC1s. Data are mean ± s.e.m. fold change over control, $n = 3$; $^{**}P = 0.0017$ (**t**), $^{***}P = 0.0003$ (**u**), $^{*}P = 0.0271$ (**v**) and $^{**}P = 0.0074$ (**w**); one-way ANOVA.

and proteins (IL-6Rα and GP130) (Extended Data Fig. 2s) in *Stat3*$^{+/+}$ and *Stat3*$^{-/-}$ cDC1s. These results suggest that a paracrine-activated IL-6–STAT3 pathway regulates the GMRβ–JAK2–STAT5 signalling pathway in DCs, affecting DC phenotype in the TME.

To validate this possibility in vivo and elucidate the biological involvement of JAK2, we treated B16F10 or MC38 colon carcinoma-bearing *Stat3*$^{-/-}$ and *Stat3*$^{+/+}$ mice with the JAK2 inhibitor FLLL32. As expected, *Stat3*$^{-/-}$ cDC1s expressed higher levels of pSTAT5 (Extended Data

Fig. 2t,u) and maturation markers compared with *Stat3*$^{+/+}$ cDC1s (Extended Data Fig. 2v–x), whereas treatment with FLLL32 abolished this effect (Extended Data Fig. 2t–x). Then, we treated *Stat3*$^{-/-}$ and *Stat3*$^{+/+}$ cDC1s with the STAT5 inhibitor STAT5i[34]. We observed higher expression levels of MHCII (Fig. 2l) and IL-12 (Fig. 2m) in *Stat3*$^{-/-}$ cDC1s than in *Stat3*$^{+/+}$ cDC1s, and these effects were abolished by the STAT5i (Fig. 2l,m). Therefore, STAT3 may restrain JAK2-mediated STAT5 activation in DC1s and the functional maturation of these cells.

To complement these observations and systemically explore how STAT3 regulates DC phenotype, we conducted RNA-seq analysis of *Stat3*$^{+/+}$ and *Stat3*$^{-/-}$ cDC1s. We observed a noticeable difference in the expression levels of maturation- and function-related genes between *Stat3*$^{+/+}$ and *Stat3*$^{-/-}$ cDC1s (Fig. 2n,o). Gene set enrichment analysis (GSEA) also showed a positive enrichment of maturation and function signatures in differentially expressed genes in *Stat3*$^{-/-}$ cDC1s relative to *Stat3*$^{+/+}$ cDC1s, including antigen processing and presentation (Fig. 2p), IL-12 production (Fig. 2q), CCR chemokine receptor binding (Extended Data Fig. 2y) and IFNγ-production pathways (Extended Data Fig. 2z). Consistently, the top upregulated canonical pathways in response to lipopolysaccharide (LPS) in *Stat3*$^{-/-}$ cDC1s compared with *Stat3*$^{+/+}$ cDC1s included antigen presentation, DC maturation and interferon signalling (Fig. 2r). Differential gene expression analysis revealed that genes associated with the STAT5 pathway were upregulated with LPS treatment in *Stat3*$^{-/-}$ cDC1s compared with *Stat3*$^{+/+}$ cDC1s (Fig. 2s). Furthermore, STAT5 chromatin immunoprecipitation followed by quantitative PCR (ChIP–qPCR) analysis revealed enhanced STAT5 binding at the promoter sites of *H2-D1* (Fig. 2t), *H2-Eb1* (Fig. 2u), *Cd80* (Fig. 2v) and *Cd86* (Fig. 2w) in *Stat3*$^{-/-}$ cDC1s compared with *Stat3*$^{+/+}$ cDC1s. Thus, STAT3 inhibits DC1 maturation and function in a JAK2–STAT5-dependent transcriptional manner.

STAT3 dampens DC1-mediated tumour immunity

We next investigated the role of STAT3 in DC1-mediated anti-tumour response. We primed OT-I cells with *Stat3*$^{+/+}$ and *Stat3*$^{-/-}$ cDC1s with the SIINFEKL peptide (Fig. 3a–d) or without antigen (Extended Data Fig. 3a–d), and subsequently assessed T cell response. We observed that *Stat3*$^{-/-}$ cDC1s induced increased proliferation (Fig. 3a), effector cytokine expression (Fig. 3b,c) and GZMB production (Fig. 3d) compared with *Stat3*$^{+/+}$ cDC1s. These effects were not observed in the absence of SIINFEKL peptide-loaded cDC1s (Extended Data Fig. 3a–d).

To explore the in vivo effect of STAT3 on DCs in response to tumour challenge, we inoculated MC38 cells subcutaneously into *Stat3*$^{+/+}$ and *Stat3*$^{-/-}$ mice. Loss of STAT3 in cDC1s resulted in reduced tumour progression compared with *Stat3*$^{+/+}$ mice, as indicated by tumour size (Fig. 3e,f) and mass (Fig. 3g). To examine whether STAT3 deficiency affected STAT5 activation in intratumoral cDC1s, we gated on tumour-infiltrating cDC1s and detected higher levels of STAT5 activation in *Stat3*$^{-/-}$ cDC1s than in *Stat3*$^{+/+}$ cDC1s (Fig. 3h–j and Extended Data Fig. 3e). Genetic deletion of STAT3 in cDC1s led to a marked increase in the interaction between JAK2 and STAT5 in cDC1s in the TME (Extended Data Fig. 3f). *Stat3*$^{-/-}$ cDC1s in the TME (Fig. 3k–n) and tumour-draining lymph nodes (TDLNs) (Extended Data Fig. 3g–j) exhibited higher expression levels of MHCII and CD86 compared with *Stat3*$^{+/+}$ cDC1s. This was accompanied by enhanced effector T cell responses in the TME and TDLN, as indicated by higher percentages of IL-2^{+} (Extended Data Fig. 3k–o), IFNγ^{+} (Fig. 3o,p and Extended Data Fig. 3p,q) and GZMB^{+} (Fig. 3q,r) CD8^{+} T cells in *Stat3*$^{-/-}$ mice compared with *Stat3*$^{+/+}$ mice.

We extended our studies to B16F10 melanoma, a less immunogenic type of tumour. Again, B16F10 tumours progressed more slowly in *Stat3*$^{-/-}$ mice compared with *Stat3*$^{+/+}$ mice (Fig. 3s,t). B16F10 tumour-infiltrating *Stat3*$^{-/-}$ cDC1s exhibited higher levels of maturation and function markers compared with *Stat3*$^{+/+}$ cDC1s (Fig. 3u–x and Extended Data Fig. 3r–u). Moreover, we also observed higher percentages of IFNγ^{+} (Fig. 3y), GZMB^{+} (Fig. 3z), IL-2^{+} (Extended Data Fig. 3v,w) and TNF^{+} (Extended Data Fig. 3x,y) CD8^{+} T cells in the TME in *Stat3*$^{-/-}$ mice than in *Stat3*$^{+/+}$ mice. Thus, STAT3 deficiency in DCs enhances T cell function, leading to improved tumour control in vivo.

STAT3 degraders for treatment of advanced tumours

STAT3 has been pursued as a cancer therapeutic target[5,35]. Small-molecule inhibitors or oligonucleotides have been developed to target STAT3[5], with limited clinical success[35]. An indirect strategy to target STAT3 is through inhibition of JAK2 activity, such as with pacritinib[5]. However, JAK2 inhibition may affect the positive effects of STAT5 on DC1s (as we show here) and T cells[24]. Thus, we used SD-36, a highly selective and effective PROTAC degrader of the STAT3 protein[36] (Extended Data Fig. 4a). We treated cDC1s with SD-36 and observed a dose-dependent reduction in the amount of STAT3 protein (Fig. 4a). Next, we treated *Stat3*$^{+/+}$ and *Stat3*$^{-/-}$ cDC1s and subsequently stimulated them with LPS. We observed enhanced STAT5 activation in *Stat3*$^{+/+}$ cDC1s treated with SD-36 (Fig. 4b). Knocking out *Stat3* led to increased STAT5 activation, and the addition of SD-36 did not further increase STAT5 activation in *Stat3*$^{-/-}$ cDC1s (Fig. 4b). To pharmacologically validate our genetic studies on the role of STAT3 in DCs (Fig. 2 and Extended Data Fig. 2), we performed a reciprocal co-immunoprecipitation assay with anti-GMRβ and anti-JAK2 in cDC1s treated with SD-36. Pharmacological degradation of STAT3 by SD-36 led to a dose-dependent increase in the interaction between GMRβ and STAT5 (Fig. 4c) and between JAK2 and STAT5 (Fig. 4d). Moreover, DCs treated with SD-36 exhibited increased expression of MHCI (Fig. 4e,f), MHCII (Fig. 4g,h), CD80 (Fig. 4i,j) and CD86 (Fig. 4k,l) compared with the control group. As genetically knocking down STAT3 caused a slight increase in pSTAT1 in JAWSII cells (Fig. 2a), we tested whether STAT1 is involved in SD-36-mediated modification of DC phenotype. Knocking down STAT1 (Extended Data Fig. 4b) had no effect on the expression of MHCI (Extended Data Fig. 4c), MHCII (Extended Data Fig. 4d) or CD80 (Extended Data Fig. 4e) compared with the control group, and SD-36 remained equally effective in enhancing the expression of these DC maturation molecules in sh*Stat1* JAWSII cells and wild-type JAWSII cells (Extended Data Fig. 4c–e). Genetic deletion of STAT1 (Extended Data Fig. 4f) had no effect on STAT5 activation in cDC1s (Extended Data Fig. 4g), as shown in *Stat1*$^{+/+}$ and *Stat1*$^{-/-}$ cDC1s. *Stat1*$^{+/+}$ and *Stat1*$^{-/-}$ cDC1s expressed similarly high levels of MHCI, MHCII and CD80 in response to SD-36 (Extended Data Fig. 4h–j). Thus, depletion of STAT3 improves DC function via STAT5 activation.

We examined the role of SD-36 in the tumour immune response in vivo. We inoculated B16F10 melanoma into C57BL/6J mice and treated them with different doses of SD-36. SD-36 at 10 mg kg^{-1} moderately but significantly slowed down B16F10 tumour progression compared with controls (Extended Data Fig. 4k). We observed a marked inhibitory effect of SD-36 at 20 mg kg^{-1} on tumour growth in mice bearing 4T1 mammary carcinoma (Fig. 4m), MC38 colon carcinoma (Fig. 4n and Extended Data Fig. 4l,m), ID8 ovarian cancer (Fig. 4o) or Lewis lung carcinoma (LLC) (Fig. 4p). Consistently, we observed that mice treated with SD-36 at 100 mg kg^{-1} also exhibited a slower rate of progression of B16F10, CT26 and EMT6 tumours compared with the control group (Extended Data Fig. 4n–p) and had no obvious effect on the body weight of these mice (Extended Data Fig. 4q–s). Thus, SD-36 monotherapy attenuates the growth of multiple tumours including LLC, an ICB-resistant tumour[37]. Large, metastatic cancers are often resistant to ICB[38,39]. We initiated the treatment with SD-36 in CT26 tumour-bearing mice with tumour volumes greater than 500 mm^{3}. Of note, SD-36 remained therapeutically effective at this late stage (Fig. 4q and Extended Data Fig. 4t,u) as shown by increased mouse survival compared with the control group (Fig. 4r). Finally, we treated 4T1 metastatic tumour-bearing mice with SD-36. This treatment effectively reduced metastatic 4T1 tumour volume (Fig. 4s,t). Thus, SD-36 monotherapy is effective in treating advanced, metastatic and ICB-resistant cancers.

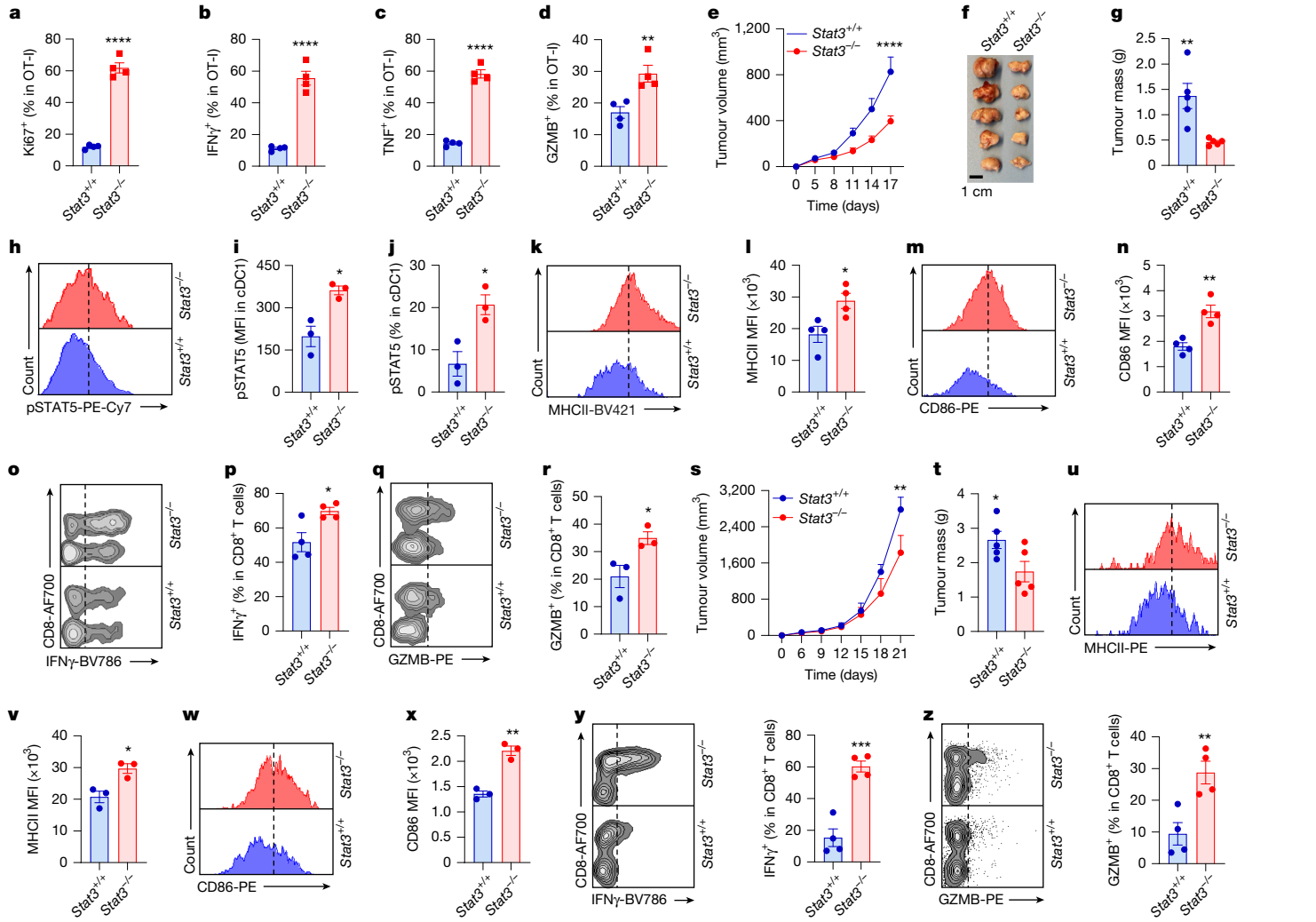

Fig. 3 | STAT3 dampens DC1-mediated immunity. a–d, OT-I cells were cultured with *Stat3*$^{+/+}$ or *Stat3*$^{-/-}$ cDC1s in the presence of SIINFEKL peptides. **a–d**, FACS analysis of Ki-67^{+} (**a**), IFNγ^{+} (**b**), TNF^{+} (**c**) and GZMB^{+} (**d**) T cells. Data are mean ± s.e.m., $n = 4$; ****$P < 0.0001$ (**a–c**) and **$P = 0.009$ (**d**), unpaired two-tailed *t*-test. **e–r**, MC38 tumours were inoculated into *Stat3*$^{+/+}$ and *Stat3*$^{-/-}$ mice. **e–g**, Tumour volume (**e**), images (**f**) and mass (**g**). **h–r**, FACS analysis of pSTAT5 (**h–j**), MHCII (**k**,**l**) and CD86 (**m**,**n**) in tumour-infiltrating cDC1s, and the percentage of tumour-infiltrating IFNγ^{+} (**o**,**p**) and GZMB^{+} (**q**,**r**) CD8^{+} T cells. One representative flow histogram or dot plot is shown (**h**,**k**,**m**,**o**,**q**). Data are mean ± s.e.m., $n = 5$ (**e**,**g**), $n = 3$ (**i**,**j**,**r**) and $n = 4$ (**l**,**n**,**p**); ****$P < 0.0001$ (**e**) **$P = 0.0067$ (**g**), *$P = 0.0144$ (**i**), *$P = 0.0198$ (**j**), *$P = 0.0231$ (**l**), **$P = 0.003$ (**n**), *$P = 0.0223$ (**p**) and *$P = 0.0405$ (**r**); two-way ANOVA (**e**), unpaired two-tailed *t*-test (**g**,**i**,**j**,**l**,**n**,**p**,**r**). **s–z**, B16F10 tumours were inoculated into *Stat3*$^{+/+}$ and *Stat3*$^{-/-}$ mice. **s**,**t**, Tumour volume (**s**) and mass (**t**). **u–z**, FACS analysis of MHCII (**u**,**v**) and CD86 (**w**,**x**) in tumour-infiltrating cDC1s, and the percentage of tumour-infiltrating IFNγ^{+} (**y**) and GZMB^{+} (**z**) CD8^{+} T cells. One representative flow histogram or dot plot is shown (**u**,**w**,**y**,**z**). Data are mean ± s.e.m., $n = 5$ (**s**,**t**), $n = 3$ (**v**,**x**) and $n = 4$ (**y**,**z**); **$P = 0.0018$ (**s**), *$P = 0.045$ (**t**), *$P = 0.0197$ (**v**), **$P = 0.0015$ (**x**), ***$P = 0.0005$ (**y**) and **$P = 0.0085$ (**z**); two-way ANOVA (**s**), unpaired two-tailed *t*-test (**t**,**v**,**x–z**).

STAT3 degradation in DCs boosts immunity

We next studied whether the anti-tumour effect of SD-36 was immune- and/or DC-dependent. To this end, we treated MC38 tumour-bearing NOD.SCID γc^{null} (NSG) mice with a low dose of SD-36 (20 mg kg^{-1}). This dose of SD-36 had no effect on tumours, as shown by tumour volume (Fig. 5a) and mass (Fig. 5b) in NSG mice. A high dose of SD-36 (100 mg kg^{-1}) had a modest but significant inhibitory effect on tumour progression in NSG mice (Extended Data Fig. 5a). Given that both innate and adaptive immunity are deficient in NSG mice, we treated MC38-bearing *Rag1*$^{-/-}$ mice, which have functional innate immunity, with SD-36. Similarly, a low dose of SD-36 (20 mg kg^{-1}) did not have any effect on tumour volume (Fig. 5c), weight (Fig. 5d) or appearance (Fig. 5e) in *Rag1*$^{-/-}$ mice. Thus, the therapeutic effect of SD-36 is dependent on an intact adaptive immune system. We treated MC38-bearing wild-type mice with anti-CD8 antibody to deplete CD8^{+} T cells (Extended Data Fig. 5b). CD8^{+} T cell depletion resulted in the loss of SD-36 therapeutic effectiveness (Fig. 5f). Indeed, SD-36 treatment increased the fraction of CD8^{+} T cells that express TNF (Fig. 5g,h), IFNγ (Fig. 5i,j) and GZMB (Fig. 5k,l) in 4T1 tumours and TDLNs (Extended Data Fig. 5c–f) and LLC (Extended Data Fig. 5g–r). Thus, STAT3 degradation enhances CD8^{+} T cell-mediated anti-tumour efficacy.

To investigate whether DC1s were involved in the therapeutic efficacy of SD-36, we treated tumour-bearing *Batf3*$^{-/-}$ mice lacking cDC1s[40]. The anti-tumour efficacy of SD-36 therapy was absent in *Batf3*-deficient mice bearing MC38 (Fig. 5m), B16F10 (Fig. 5n) or LLC (Extended Data Fig. 5s) tumours. STAT3 was highly expressed in intratumoral DCs in wild-type mice bearing LLC tumours (Fig. 5o), and SD-36 treatment resulted in a rapid and efficient degradation of STAT3 protein in DCs compared with tumour cells (Extended Data Fig. 5t). Of note, the intracellular concentration of SD-36 was four times higher in DCs than in tumour cells (Extended Data Fig. 5u). These results suggest that SD-36 effectively induces degradation of STAT3 in DCs to achieve its therapeutic efficacy in vivo.

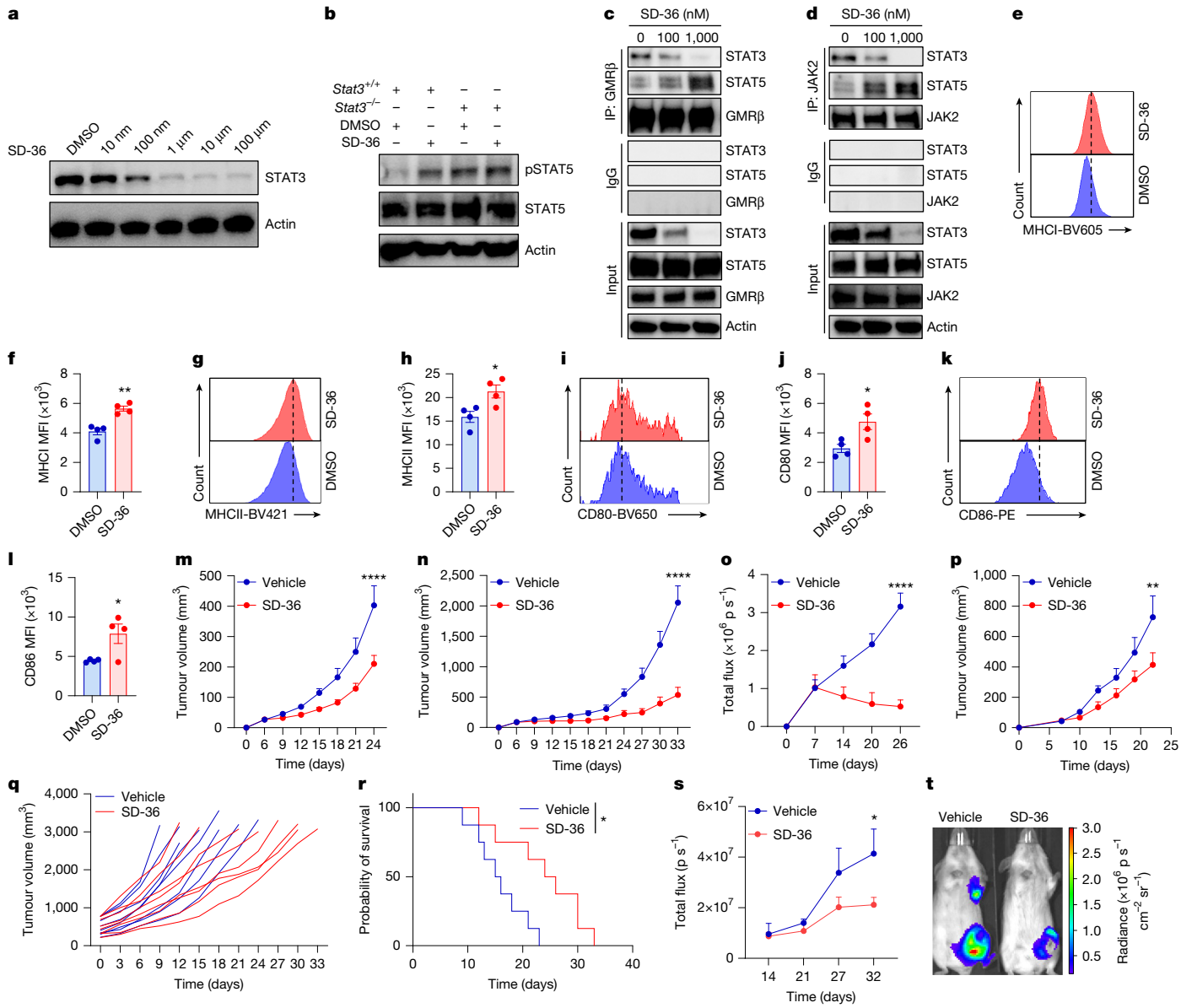

Fig. 4 | STAT3 degraders for treatment of advanced tumours. a, Immunoblot showing STAT3 expression in mouse cDC1s treated with different concentrations of SD-36 in vitro. **b**, Immunoblot showing expression of pSTAT5 and STAT5 in cDC1s from *Stat3*$^{+/+}$ and *Stat3*$^{-/-}$ mice treated with SD-36 (200 nM) for 48 h and LPS (20 ng ml^{-1}) for 1 h. In **a**,**b**, one of three experiments is shown. **c**,**d**, cDC1s were treated with different doses of SD-36 for 24 h and were immunoprecipitated (IP) with anti-GMRβ (**c**) or anti-JAK2 (**d**). The immunoprecipitation shows the interaction between GMRβ, JAK2, STAT3 and STAT5 in cDC1s. One of two experiments with repeats is shown. **e**–**l**, FACS analysis of MHCI (**e**,**f**), MHCII (**g**,**h**), CD80 (**i**,**j**) and CD86 (**k**,**l**) on cDC1s treated with SD-36 (**e**–**h**) and SD-36 plus LPS (**i**–**l**). Representative histograms are shown. Data are mean ± s.e.m., $n = 4$; $^{*}P = 0.0241$ (**h**), $^{*}P = 0.023$ (**j**), $^{*}P = 0.0329$ (**l**) and $^{**}P = 0.0015$ (**f**), unpaired two-tailed *t*-test. **m**–**p**, Mice were inoculated with 4T1 (**m**), MC38 (**n**), ID8 (**o**) or LLC (**p**) cells and were treated with SD-36 (20 mg kg^{-1}) every 3 days, and tumour volumes were monitored. Data are mean ± s.e.m.; $n = 6$ (**m**,**p**) and $n = 5$ (**n**,**o**); $^{**}P = 0.0021$ (**p**) and $^{****}P < 0.0001$ (**m**–**o**), two-way ANOVA. **q**–**r**. Mice bearing CT26 tumours (500 mm^3 per tumour) were treated with SD-36 or vehicle and tumour volumes (**q**) and mouse survival (**r**) were monitored. Data are mean ± s.e.m.; $n = 8$; $^{*}P = 0.0111$ (**r**), log-rank test. **s**,**t**, Luciferase radiance images (**s**) and total fluxes of metastatic 4T1 tumours (**t**) from mice treated with SD-36. Data are mean ± s.e.m.; vehicle: $n = 5$, SD-36: $n = 6$; $^{*}P = 0.0348$, two-way ANOVA.

Next, we found that SD-36 treatment reduced pSTAT3 and increased pSTAT5 in MC38 tumour-infiltrating cDC1s (Fig. 5p–r). We also observed enhanced STAT5 activation in DCs isolated from the spleens of MC38-bearing mice after SD-36 treatment (Extended Data Fig. 5v). SD-36 treatment increased DC maturation and function markers in cDC1s in B16F10 tumours (Fig. 5s–u).

We examined whether STAT3 in DCs is a direct functional target of SD-36 therapy in vivo in tumour-bearing mice. We treated B16F10-bearing *Stat3*$^{+/+}$ and *Stat3*$^{-/-}$ mice with SD-36. SD-36 treatment inhibited tumour growth in *Stat3*$^{+/+}$ mice, whereas this effect was abolished in *Stat3*$^{-/-}$ mice (Fig. 5v). Similar results were observed in MC38 tumour-bearing mice (Extended Data Fig. 5w). We next transferred *Stat3*$^{+/+}$ or *Stat3*$^{-/-}$ cDC1s into B16F10 or MC38 tumour-bearing *Batf3*$^{-/-}$ mice and treated these mice with SD-36. Again, SD-36 improved the anti-tumour effect in *Batf3*$^{-/-}$ mice that received *Stat3*$^{+/+}$ cDC1s, but not in those that received *Stat3*$^{-/-}$ cDC1s (Fig. 5w, Extended Data Fig. 5x).

We used STAT5i[34] to assess the interplay between STAT3 and STAT5 in DCs (Fig. 2l,m). STAT5i can have off-target effects. To genetically validate whether STAT5 in DCs contributes to SD-36-mediated anti-tumour immunity, we transferred *Stat5b*$^{-/-}$ cDC1s or *Stat5b*$^{+/+}$ cDC1s into MC38

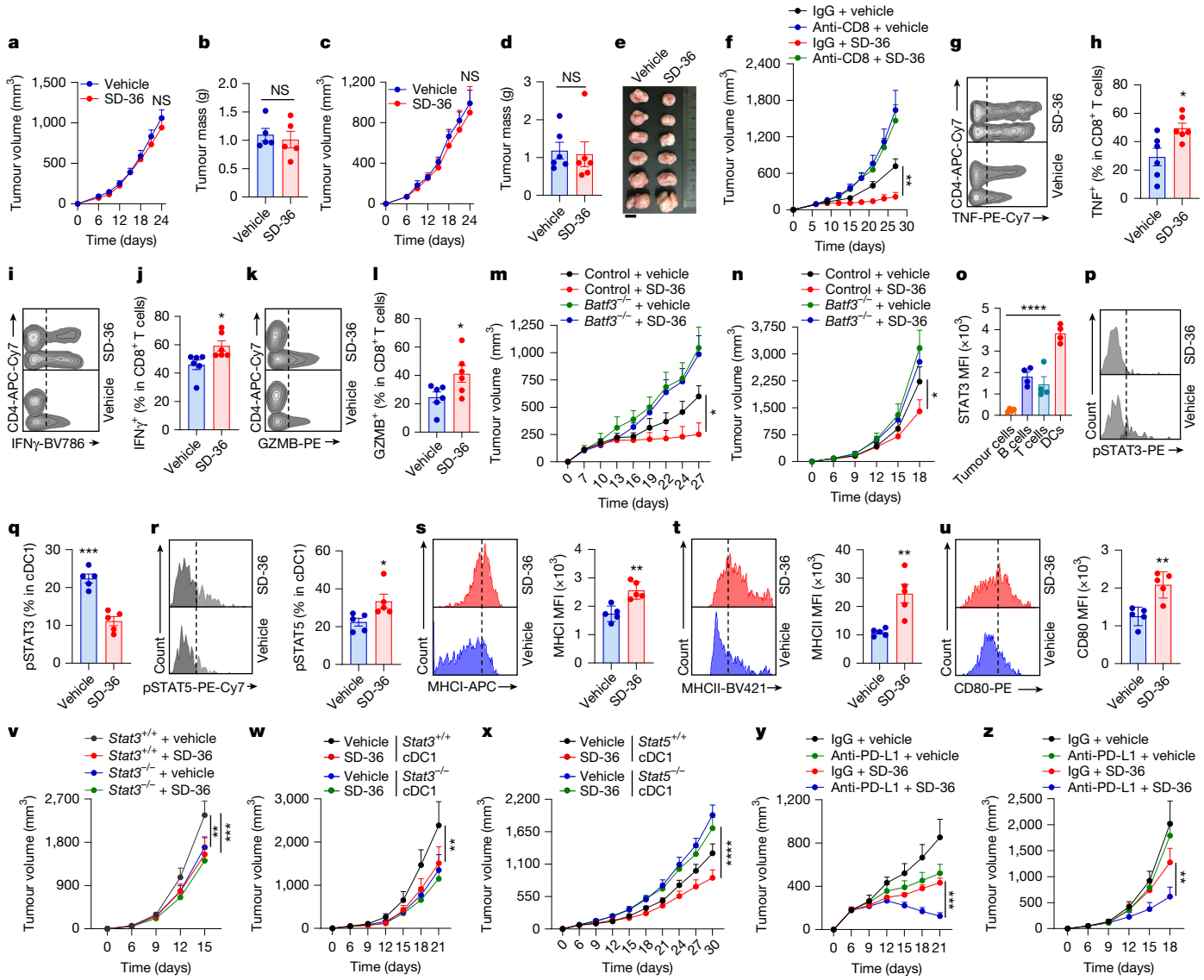

Fig. 5 | STAT3 degradation in DCs boosts immunity. a–**e**, Tumours in MC38-bearing NSG (**a**,**b**) and *Rag1*$^{-/-}$ mice (**c**–**e**) treated with SD-36 were monitored. $n = 5$ (**a**,**b**) and n = 6 (**c**,**d**); two-way ANOVA (**a**,**c**) and unpaired two-tailed *t*-test (**b**,**d**). Scale bar, 1 cm. NS, not significant. **f**, Tumour volume was monitored in MC38-bearing mice treated as indicated. Data are mean ± s.e.m., $n = 6$; $^{**}P = 0.0018$, two-way ANOVA. **g**–**l**, FACS analysis of 4T1-infiltrating TNF$^+$ (**g**,**h**), IFNγ$^+$ (**i**,**j**) and GZMB$^+$ (**k**,**l**) CD8$^+$ T cells from mice treated with SD-36. Data are mean ± s.e.m., $n = 6$; $^{*}P = 0.0175$ (**h**), $^{*}P = 0.0232$ (**j**) and $^{*}P = 0.0404$ (**l**), unpaired two-tailed *t*-test. **m**,**n**, Tumour volumes were monitored in *Batf3*$^{-/-}$ and wild-type mice bearing MC38 (**m**) or B16F10 (**n**) tumours and treated with SD-36. Data are mean ± s.e.m.; $n = 5$ (**m**), and $n = 8$ (**n**); $^{*}P = 0.0158$ (**m**) and $^{*}P = 0.0126$ (**n**), two-way ANOVA. **o**, FACS analysis of STAT3 expression in different cell types from LLC-bearing mice. Data are mean ± s.e.m., $n = 4$; $^{****}P < 0.0001$, one-way ANOVA. **p**–**r**, FACS analysis of pSTAT3 (**p**,**q**) and pSTAT5 (**r**) in MC38-infiltrating cDC1s from mice treated with SD-36. Data are mean ± s.e.m., $n = 5$; $^{*}P = 0.0335$ and $^{***}P = 0.0002$, unpaired two-tailed *t*-test. **s**–**u**, FACS analysis of MHCI (**s**), MHCII (**t**) and CD80 (**u**) in B16F10-infiltrating cDC1s from mice treated with SD-36. Data are mean ± s.e.m., $n = 5$; $^{**}P = 0.0021$ (**s**), $^{**}P = 0.0035$ (**t**) and $^{**}P = 0.0023$ (**u**), unpaired two-tailed *t*-test. **v**, Tumour volume in B16F10-bearing *Stat3*$^{+/+}$ and *Stat3*$^{-/-}$ mice treated with SD-36. Data are mean ± s.e.m., $n = 7$; $^{**}P = 0.0067$ and $^{***}P = 0.0006$, two-way ANOVA. **w**, B16F10-bearing *Batf3*$^{-/-}$ mice were transferred with *Stat3*$^{+/+}$ and *Stat3*$^{-/-}$ cDC1s and treated with SD-36, and tumour volume was monitored. Data are mean ± s.e.m., $n = 7$; $^{**}P = 0.0094$, two-way ANOVA. **x**, *Stat5*$^{+/+}$ and *Stat5*$^{-/-}$ cDC1s were transferred into MC38-bearing *Batf3*$^{-/-}$ mice, treated with SD-36, and tumour volume was monitored. Data are mean ± s.e.m., $n = 7$; $^{****}P < 0.0001$, two-way ANOVA. **y**,**z**, Tumour volume was monitored in mice bearing MC38 (**y**) and B16F10 (**z**) tumours and treated as indicated. Data are mean ± s.e.m.; $n = 6$ (**y**) and $n = 7$ (**z**); $^{**}P = 0.0094$ (**z**) and $^{***}P = 0.0009$ (**y**), two-way ANOVA.

tumour-bearing *Batf3*$^{-/-}$ mice and treated these mice with SD-36. SD-36 effectively controlled tumour progression in mice receiving *Stat5b*$^{+/+}$ cDC1s, but not *Stat5b*$^{-/-}$ cDC1s (Fig. 5x). Therefore, SD-36 reprograms key transcription factors in cDC1s by degrading STAT3 and enhancing STAT5 signalling, thereby inducing potent anti-tumour immunity in vivo.

Finally, we examined whether SD-36 could synergize with ICB. To this end, we treated mice bearing MC38 or B16F10 tumours with PD-L1 monoclonal antibody, SD-36 or both. Anti-PD-L1 inhibited MC38 tumour growth but had no effect on B16F10 tumours, whereas SD-36 monotherapy efficiently slowed down MC38 and B16F10 tumour growth. The combined treatment profoundly inhibited progression of MC38 and B16F10 tumours (Fig. 5y,z). We further tested SD-36 in human DC-mediated T cell activation in the context of ICB. We isolated DCs from fresh human ovarian cancer tissues and treated these DCs with SD-36 and/or anti-human PD-L1 monoclonal antibody, and co-cultured these DCs with T cells. Treatment with SD-36 or anti-PD-L1 increased the numbers of polyfunctional human T cells, as shown by

GZMB$^+$IFNγ$^+$ (Extended Data Fig. 6a). The combined treatment additionally upregulated the levels of polyfunctional T cells (Extended Data Fig. 6a,b).

To further investigate degradation of STAT3 as a potential immunotherapeutic strategy, we have developed SD-2301, another highly potent and selective STAT3 degrader (Extended Data Fig. 6c). In contrast to SD-36, which engaged the cereblon–cullin 4A complex for induced STAT3 degradation, SD-2301 used a high-affinity VHL ligand to recruit VHL–cullin 2 for STAT3 degradation. SD-2301 effectively degraded STAT3 in DCs in vitro (Extended Data Fig. 6d). Treatment with SD-2301 resulted in a potent STAT3 degradation in DCs in vivo in B16F10 tumour-bearing mice (Extended Data Fig. 6e). Of note, SD-2301 exhibited four- to five-fold improved potency compared with SD-36 towards STAT3 degradation in DCs (Extended Data Fig. 6f). An efficacy experiment showed that 5 mg kg^{-1} SD-2301 was effective in reducing B16 tumour progression and was four times more potent than SD-36 (Extended Data Fig. 6g). Treatment with SD-2301 also increased the number of effector CD8$^+$ T cells, as shown by IFNγ (Extended Data Fig. 6h,i) and GZMB (Extended Data Fig. 6j,k) expression. In line with this, SD-2301 treatment increased DC maturation and function markers in cDC1s in B16F10 tumours (Extended Data Fig. 6l–n). Treatment with SD-2301 had no effect on CD31$^+$ blood vessel densities in B16F10 (Extended Data Fig. 6o) and MC38 (Extended Data Fig. 6p) tumour tissues and did not affect the body weight of mice bearing B16F10 tumours (Extended Data Fig. 6q).

In addition, whereas anti-PD-L1 monotherapy had no effect on B16F10 tumour growth, combined SD-2301 and anti-PD-L1 synergistically inhibited tumour growth (Extended Data Fig. 6r). In the MC38 tumour model, anti-PD-L1 or SD-2301 monotherapy effectively inhibited tumour growth, and the combined therapy profoundly suppressed MC38 tumour progression (Extended Data Fig. 6s). Accordingly, SD-2301 treatment increased the proportion of MC38 tumour neoantigen-specific (KSPWFTTL) tetramer$^+$CD8$^+$ T cells compared with the control treatment (Extended Data Fig. 6t,u). These results highlight that SD-2301 may enhance DC-mediated antigen specific T cell priming and presentation in vivo.

Next, we explored whether DC1s and STAT3 are direct cellular and molecular targets of SD-2301 therapy in vivo. To address this, we treated B16F10-bearing *Stat3*$^{+/+}$ and *Stat3*$^{-/-}$ mice with SD-2301. As expected, SD-2301 treatment inhibited tumour growth in *Stat3*$^{+/+}$ mice, whereas this effect was abolished in *Stat3*$^{-/-}$ mice (Extended Data Fig. 6v). The anti-tumour efficacy of SD-2301 therapy was absent in *Batf3*-deficient mice bearing MC38 tumours (Extended Data Fig. 6w). These results indicate that cDC1s have a key role in the therapeutic efficacy of SD-2301 in vivo.

Pharmacokinetic evaluation showed that SD-2301 had an excellent pharmacokinetic profile in mice, as characterized by a slow clearance and high plasma exposure (Extended Data Fig. 6x). Moreover, SD-2301 was highly potent and selective in inducing degradation of STAT3 over all other STAT proteins in human peripheral blood monocyte cells in vitro (Extended Data Fig. 6y). Together, our results suggest that STAT3 serves as a brake to restrain JAK2-mediated STAT5 activation in DCs and STAT3 degradation in DCs elicits potent anti-tumour immunity, thereby being a promising approach for cancer immunotherapy (Extended Data Fig. 6z).

Discussion

This study offers support for several undocumented perspectives in the field of tumour immunology and immunotherapy. First, STAT3 counteracts STAT5 activation, which restrains DC maturation in the TME. Second, STAT3 degradation is a potential immunotherapeutic modality for treating patients with advanced and ICB-resistant cancer. Third, STAT3 degraders work in an DC-dependent manner, supporting STAT5-mediated DC maturation and function.

DCs prime and activate T cells against cancer cells[3,41,42]. We found that ICB can reprogram the STAT5 and STAT3 transcriptional pathways in DCs, thereby normalizing DC function in the TME. It has long been thought that DCs are potential immunotherapeutic targets. However, it is challenging to therapeutically manipulate DCs owing to their numeric scarcity, subset diversity and lack of specific molecular targets. Our results suggest that STAT3 is a druggable molecular target in DC1s using our potent and highly selective PROTAC STAT3 degraders.

Despite the identification of STAT3 and STAT5 many years ago[20,43–45], the interplay between STAT3 and STAT5 signalling pathways in specific immune cells remain poorly understood. STAT3 is frequently activated in the TME owing to abundant stimulating factors, including IL-6, IL-10 and VEGF[20,21], whereas STAT5 is often activated by T cell-derived cytokines, such as GM-CSF and IL-2. Given that T cells are limited or dysfunctional in the TME, the balance between STAT5 and STAT3 in immune cells, including DCs, may be biased towards STAT3 overactivation. In support of this possibility, we demonstrate that there is an imbalance between these two transcriptional pathways in DC1s in the TME, tilting towards an activation in STAT3 over STAT5. At the molecular level, DC1s express high levels of GM-CSF receptor and the STAT3 transcriptional signalling pathway restrains the GMR–JAK2–STAT5 signalling axis in DCs in the TME. The interaction between GMR and JAK2 appears to regulate both the STAT3 and STAT5 transcriptional pathways in DC1s. In support of this possibility, we observed that GM-CSF stimulation or genetically knocking down GM-CSF receptor alters the phosphorylation of JAK2, STAT3 and STAT5, but not JAK1, JAK3, TYK2 and STAT1 in cDC1s. Of note, targeting STAT3 has no effect on the expression levels of GM-CSF and GMRβ but enhances the interaction of GMRβ and JAK2 with STAT5, leading to the phosphorylation of STAT5 and DC maturation. Therefore, STAT3 restrains JAK2-mediated STAT5 activation in DCs, thereby impairing DC1-mediated T cell immunity.

To rescue the STAT3-impaired DC phenotype, we developed two PROTAC molecules (SD-36 and SD-2301) that target STAT3 protein for degradation. There are several key functional characteristics of our STAT3 degraders. First, they are highly selective and efficacious in degrading STAT3. Second, low doses of SD-36 and SD-2301 effectively target DCs. Furthermore, low doses of SD-36 and SD-2301 mediate an immune-dependent anti-tumour effect, whereas high doses of SD-36 can directly control tumour progression in the absence of a functional immune system[36]. Intriguingly, SD-36 or SD-2301, as a monotherapy, exhibit remarkable efficacy in treating large, advanced tumours and ICB-resistant tumours. Given that the anti-tumour effect of SD-2301 is four to five times more potent than that of SD-36 in degrading STAT3 and it has excellent pharmacokinetics, we are evaluating SD-2301 as a potential drug candidate for clinical development. Notably, although STAT3 degraders efficaciously target DCs, the involvement of STAT3 in other cell types may also influence immune responses in the TME. Together, our study provides strong support for potential human clinical trials of STAT3 degraders in treating patients with large and metastatic tumours and/or ICB-resistant tumours.

Online content

Any methods, additional references, Nature Portfolio reporting summaries, source data, extended data, supplementary information, acknowledgements, peer review information; details of author contributions and competing interests; and statements of data and code availability are available at https://doi.org/10.1038/s41586-025-09000-3.

1. Sharma, P. & Allison, J. P. The future of immune checkpoint therapy. *Science* **348**, 56–61 (2015).
2. Zou, W., Wolchok, J. D. & Chen, L. PD-L1 (B7-H1) and PD-1 pathway blockade for cancer therapy: mechanisms, response biomarkers, and combinations. *Sci. Transl. Med.* **8**, 328rv324 (2016).
3. Wculek, S. K. et al. Dendritic cells in cancer immunology and immunotherapy. *Nat. Rev. Immunol.* **20**, 7–24 (2020).

4. Spranger, S., Dai, D., Horton, B. & Gajewski, T. F. Tumor-residing Batf3 dendritic cells are required for effector T cell trafficking and adoptive T cell therapy. *Cancer Cell* **31**, 711–723 (2017).
5. Johnson, D. E., O'Keefe, R. A. & Grandis, J. R. Targeting the IL-6/JAK/STAT3 signalling axis in cancer. *Nat. Rev. Clin. Oncol.* **15**, 234–248 (2018).
6. June, C. H. & Sadelain, M. Chimeric antigen receptor therapy. *New Engl. J. Med.* **379**, 64–73 (2018).
7. Inaba, K., Young, J. W. & Steinman, R. M. Direct activation of $CD8^+$ cytotoxic T lymphocytes by dendritic cells. *J. Exp. Med.* **166**, 182–194 (1987).
8. Everts, B. et al. Migratory $CD103^+$ dendritic cells suppress helminth-driven type 2 immunity through constitutive expression of IL-12. *J. Exp. Med.* **213**, 35–51 (2016).
9. Maier, B. et al. A conserved dendritic-cell regulatory program limits antitumour immunity. *Nature* **580**, 257–262 (2020).
10. Anderson, D. A. 3rd, Dutertre, C. A., Ginhoux, F. & Murphy, K. M. Genetic models of human and mouse dendritic cell development and function. *Nat. Rev. Immunol.* **21**, 101–115 (2021).
11. Duong, E. et al. Type I interferon activates MHC class I-dressed $CD11b^+$ conventional dendritic cells to promote protective anti-tumor $CD8^+$ T cell immunity. *Immunity* **55**, 308–323 (2022).
12. Ganesan, A. P. et al. Tissue-resident memory features are linked to the magnitude of cytotoxic T cell responses in human lung cancer. *Nat. Immunol.* **18**, 940–94 (2017).
13. Bottcher, J. P. et al. NK cells stimulate recruitment of cDC1 into the tumor microenvironment promoting cancer immune control. *Cell* **172**, 1022–1037 (2018).
14. Gerhard, G. M., Bill, R., Messemaker, M., Klein, A. M. & Pittet, M. J. Tumor-infiltrating dendritic cell states are conserved across solid human cancers. *J. Exp. Med.* **218**, e20200264 (2021).
15. Salmon, H. et al. Expansion and activation of $CD103^+$ dendritic cell progenitors at the tumor site enhances tumor responses to therapeutic PD-L1 and BRAF inhibition. *Immunity* **44**, 924–938 (2016).
16. Qiao, J. et al. Targeting tumors with IL-10 prevents dendritic cell-mediated $CD8^+$ T cell apoptosis. *Cancer Cell* **35**, 901–915 (2019).
17. Guo, C. S. et al. SLC38A2 and glutamine signalling in cDC1s dictate anti-tumour immunity. *Nature* **620**, 200–20 (2023).
18. Li, Y. J., Zhang, C., Martincuks, A., Herrmann, A. & Yu, H. STAT proteins in cancer: orchestration of metabolism. *Nat. Rev. Cancer* **23**, 115–134 (2023).
19. Fu, X. Y. STAT3 in immune responses and inflammatory bowel diseases. *Cell Res.* **16**, 214–219 (2006).
20. Zhong, Z., Wen, Z. & Darnell, J. E. Jr. Stat3: a STAT family member activated by tyrosine phosphorylation in response to epidermal growth factor and interleukin-6. *Science* **264**, 95–98 (1994).
21. Yu, H., Kortylewski, M. & Pardoll, D. Crosstalk between cancer and immune cells: role of STAT3 in the tumour microenvironment. *Nat. Rev. Immunol.* **7**, 41–51 (2007).
22. Liao, W., Lin, J. X., Wang, L., Li, P. & Leonard, W. J. Modulation of cytokine receptors by IL-2 broadly regulates differentiation into helper T cell lineages. *Nat. Immunol.* **12**, 551–U247 (2011).
23. Eddy, W. E. et al. Stat5 is required for $CD103^+$ dendritic cell and alveolar macrophage development and protection from lung injury. *J. Immunol.* **198**, 4813–4822 (2017).
24. Zhou, J. et al. The ubiquitin ligase MDM2 sustains STAT5 stability to control T cell-mediated antitumor immunity. *Nat. Immunol.* **22**, 460–470 (2021).
25. Choi, J. E. et al. PIKfyve, expressed by CD11c-positive cells, controls tumor immunity. *Nat. Commun.* **15**, 5487 (2024).
26. Rosenberg, J. E. et al. Atezolizumab in patients with locally advanced and metastatic urothelial carcinoma who have progressed following treatment with platinum-based chemotherapy: a single-arm, multicentre, phase 2 trial. *Lancet* **387**, 1909–1920 (2016).
27. Yuan, X. et al. Vitamin E enhances cancer immunotherapy by reinvigorating dendritic cells via targeting checkpoint SHP1. *Cancer Discov.* **12**, 1742–1759 (2022).
28. Van Allen, E. M. et al. Genomic correlates of response to CTLA-4 blockade in metastatic melanoma. *Science* **350**, 207–211 (2015).
29. Gide, T. N. et al. Distinct immune cell populations define response to anti-PD-1 monotherapy and anti-PD-1/anti-CTLA-4 combined therapy. *Cancer Cell* **35**, 238–255 (2019).
30. Zhang, Y. et al. Single-cell analyses reveal key immune cell subsets associated with response to PD-L1 blockade in triple-negative breast cancer. *Cancer Cell* **39**, 1578–1593 (2021).
31. Theisen, D. J. et al. WDFY4 is required for cross-presentation in response to viral and tumor antigens. *Science* **362**, 694–69 (2018).
32. Choi, H. W. et al. Perivascular dendritic cells elicit anaphylaxis by relaying allergens to mast cells via microvesicles. *Science* **362**, 656–65 (2018).
33. Al-Shami, A., Mahanna, W. & Naccache, P. H. Granulocyte-macrophage colony-stimulating factor-activated signaling pathways in human neutrophils—selective activation of Jak2, Stat3, and Stat5B. *J. Biol. Chem.* **273**, 1058–1063 (1998).
34. Riggan, L. et al. The transcription factor Fli1 restricts the formation of memory precursor NK cells during viral infection. *Nat. Immunol.* **23**, 556–55 (2022).
35. Huynh, J., Chand, A., Gough, D. & Ernst, M. Therapeutically exploiting STAT3 activity in cancer - using tissue repair as a road map. *Nat. Rev. Cancer* **19**, 82–96 (2019).
36. Bai, L. et al. A potent and selective small-molecule degrader of STAT3 achieves complete tumor regression in vivo. *Cancer Cell* **36**, 498–511 (2019).
37. Lin, H. et al. Host expression of PD-L1 determines efficacy of PD-L1 pathway blockade-mediated tumor regression. *J. Clin. Invest.* **128**, 805–815 (2018).
38. Nishinol, M., Giobbie-Hurder, A., Ramaiyal, N. H. & Hodit, F. S. Response assessment in metastatic melanoma treated with ipilimumab and bevacizumab: CT tumor size and density as markers for response and outcome. *J. Immunother. Cancer* **2**, 40 (2014).
39. Yu, J. et al. Liver metastasis restrains immunotherapy efficacy via macrophage-mediated T cell elimination. *Nat. Med.* **27**, 152–164 (2021).
40. Hildner, K. et al. Batf3 deficiency reveals a critical role for $CD8\alpha^+$ dendritic cells in cytotoxic T cell immunity. *Science* **322**, 1097–1100 (2008).
41. Durai, V. & Murphy, K. M. Functions of murine dendritic cells. *Immunity* **45**, 719–736 (2016).
42. Murphy, T. L. & Murphy, K. M. Dendritic cells in cancer immunology. *Cell. Mol. Immunol.* **19**, 3–13 (2022).
43. Fu, X. Y. & Zhang, J. J. Transcription factor p91 interacts with the epidermal growth factor receptor and mediates activation of the c-fos gene promoter. *Cell* **74**, 1135–1145 (1993).
44. Sadowski, H. B., Shuai, K., Darnell, J. E. Jr. & Gilman, M. Z. A common nuclear signal transduction pathway activated by growth factor and cytokine receptors. *Science* **261**, 1739–1744 (1993).
45. Wakao, H., Gouilleux, F. & Groner, B. Mammary gland factor (MGF) is a novel member of the cytokine regulated transcription factor gene family and confers the prolactin response. *EMBO J.* **13**, 2182–2191 (1994).

Methods

Antibodies, plasmids and reagents

Western blot analyses were performed using primary antibodies at a dilution of 1:1,000 unless otherwise specified. Anti-STAT1 (D1K9Y, 14994), anti-STAT2 (D9J7L, 72604), anti-STAT3 (Rabbit, 79D7, 4904; Mouse, 124H6, 9139), anti-STAT4 (C46B10, 2653), anti-STAT5 (D2O6Y, 94205), anti-STAT6 (D3H4, 5397), anti-JAK1 (6G4, 3344), anti-JAK2 (D2E12, 3230), anti-JAK3 (D7B12, 8863), anti-TYK2 (E9H4T, 35615), anti-p65 (D14E12, 8242), anti-CD80 (E6J6N, 54521), anti-CD86 (E5W6H, 19589), anti-IL-6Rα (E7H4J, 39837), anti-GP130 (3732), anti-pSTAT1 (58D6, 9167), anti-pSTAT3 (D3A7, 9145), anti-pSTAT5 (D47E7, 4322), anti-pSTAT6 (D8S9Y, 56554), anti-pJAK1 (D7N4Z, 74129), anti-pJAK2 (C80C3, 3776), anti-pJAK3 (D44E3, 5031), anti-pp65 (93H1, 3033) and anti-β-actin (4967) were from Cell Signaling Technology. Anti-JAK2 (C-10, sc-390539), anti-GMRβ (F-12, sc-393281) and anti-β-actin (C4, sc-47778) were from Santa Cruz Biotechnology. Anti-pTYK2 (PA5-37762) was from Invitrogen. HRP horse anti-mouse IgG antibody (PI-2000, 1:5,000) and HRP goat anti-rabbit IgG (PI-1000, 1:5,000) were from Vector Laboratories.

For the in vivo experiments, anti-mouse CD8 (clone YTS 169.4, BE0117), anti-mouse PD-L1 (clone 10F.9G2, BE0101) and anti-IgG2b (clone LTF-2, BE0090) were from BioXcell. SD-36 and SD-2301 were designed and synthesized in our laboratory. FLLL32 (JAK2 inhibitor X, 5301530001) and STAT5 inhibitor (573108) were purchased from Sigma-Aldrich. Plasmids expressing shRNAs targeting *Stat3* (TRCN0000071453, TRCN0000301946), *Stat1* (TRCN0000054924), *Jak2* (TRCN0000023649, TRCN0000023651, TRCN0000023652) and *Gmrβ* (TRCN0000067025, TRCN000067026) were from Sigma-Aldrich.

Cell culture

JAWSII, 293T, B16F10, CT26, EMT6, LLC and 4T1 cells were purchased from the American Type Culture Collection (ATCC). MC38 mouse colon cancer cell line was obtained from the University of Texas Southwestern Medical Center (Y.-X. Fu). Ovarian cancer cell line luciferase-ID8 cells were previously reported[24]. All cell lines were tested for mycoplasma contamination by MycoAlert Mycoplasma Detection kit and confirmed negative for *Mycoplasma*.

The 293T cells were transfected with packaging plasmids and non-targeting lentivirus vector, or a lentivirus vector encoding shRNAs targeting *Stat3*, *Stat1*, *Jak2* or *Gmrβ*. The virus-containing supernatant was collected 48 h after transfection. JAWSII cells were transfected with the lentivirus. Then the cell lysates were analysed by immunoblotting.

Bone marrow-derived dendritic cells

Bone marrow was collected from the femurs and tibias of mice. Red blood cells were lysed using ACK lysis buffer. Bone marrow-derived DCs (BMDCs) were generated with GM-CSF (20 ng ml^{-1}) and FLT3 ligand (100 ng ml^{-1}) in IMDM (Iscove's Modified Dulbecco's Medium; Gibco, 12440-053) supplemented with 10% FBS, 1% penicillin-streptomycin and 55 μM β-mercaptoethanol for 7–10 days. BMDCs were either sorted as cDC1s (CD11c^{+}XCR1^{+}) using a FACSAria flow cytometry sorter (BD Biosciences) or purified using biotin anti-mouse XCR1 antibody (BioLegend,148212) and anti-biotin microbeads (Miltenyi Biotec, 130-090-485) following the manufacturer's protocols for subsequent experiments. Primary cell cultures were tested to be mycoplasma-free by MycoAlert Mycoplasma Detection kit.

ELISA

Culture media were collected from *Stat3*$^{+/+}$ and *Stat3*$^{-/-}$ cDC1s and centrifuged at 8,000*g* for 5 min. GM-CSF (MGM00) and IL-6 (DY406) were detected in the culture supernatants using the ELISA kit.

CD8 depletion

CD8^{+} T cells were depleted with anti-CD8 (YTS 169.4, BioXCell) antibodies. Anti-CD8 (100 μg per mouse) antibodies were injected intraperitoneally at the beginning of tumour inoculation and continuously administered every three days.

Drug cellular uptake

DCs and LLC tumour cells were treated with 1 μM SD-36 for 12 h. Then, DCs and LLC (10^6 each) were centrifuged at 1,500 rpm for 5 min at 4 °C and washed 3 times with ice-cold PBS. The pellets were resuspended in 100 μl of a 50% (v/v) water/methanol solution and subjected to 3 freeze–thaw cycles. After the final thaw cycle, these samples were centrifuged at 14,000 rpm, 4 °C for 20 min, and the supernatant were collected. All samples were submitted to the pharmacokinetics core (University of Michigan) for analysis.

Immunoprecipitation and immunoblot analysis

Cells were lysed in immunoprecipitation lysis buffer (50 mM Tris-HCl pH 7.4, 120 mM NaCl, 1 mM EDTA and 0.5% NP-40) and supplemented with Halt Protease and Phosphatase Inhibitor Cocktail (Thermo Fisher Scientific). Cells were repeatedly passed through a 21-gauge needle with sonication. Then 1,000 μg total cell lysates were incubated with the appropriate antibody (2 μg), with rotation overnight at 4 °C, followed by a 3-h incubation with Protein A/G Sepharose beads (Santa Cruz Biotechnology). Immune complexes were washed three times with wash buffer (20 mM Tris-HCl pH 7.4, 100 mM NaCl, 1 mM EDTA and 0.2% NP-40); then the immunoprecipitated proteins were denatured by the addition of sample buffer (Bio-Rad) and boiled for 10 min, resolved by SDS–PAGE, and immunoblotted with indicated antibodies.

Cells were lysed in RIPA buffer (Thermo Fisher Scientific) supplemented with Halt Protease and Phosphatase Inhibitor Cocktail (Thermo Fisher Scientific). The protein concentrations of cell lysates were determined by BCA protein assay kit (Thermo Fisher Scientific). Equivalent amounts of total cellular protein were separated by SDS–PAGE, transferred to polyvinylidene fluoride membranes, and immunoblotted with the indicated antibodies.

For phospho-antibody array cDC1s were treated with LPS (20 ng ml^{-1}) for 3 h and lysed for protein extraction. Lysates were analysed using the Proteome Profiler Phospho-Kinase Array Kit (R&D Systems, number ARY003C) according to the manufacturer's instructions. Western blotting data were processed and analysed by image lab 6.1 (Bio-Rad) and ImageJ 1.51n (NIH).

Immunohistochemistry staining

For histological analysis, tissue samples were collected, fixed in 10% formalin (Sigma) and processed for formalin-fixed paraffin-embedded tissue analysis. Four-micrometre paraffin sections underwent heat-induced epitope retrieval. Staining was performed with anti-mouse CD31 antibody (Cell Signaling Technology, D8V9E, 77699, 1:100) using an automated immunostainer (Biocare Intellipath, Biocare Medical). Sections were counterstained with haematoxylin (Biocare Medical), and slides were scanned with the Aperio AT2 Scanner (Leica Biosystems Imaging). Quantification was performed with QuPath v0.5.1.

Quantitative PCR

Total RNA was isolated from cells by column purification (RNeasy Micro Kit, Qiagen) with DNase treatment. cDNA was synthesized using the RevertAid First Strand cDNA Synthesis Kit (Thermo Fisher Scientific) with random hexamer primers. Quantitative PCR was performed on cDNA using Fast SYBR Green Master Mix (Thermo Fisher Scientific) on a QuantStudio 3 Real-Time PCR System (Thermo Fisher Scientific). Gene expression was quantified using specific primers (Extended Data Table 3). Fold changes in messenger RNA expression were calculated with the ΔΔCt method using *Actb* as an endogenous control. The results are expressed as fold changes normalized to the controls.

Synthesis of SD-2301 and its chemical data

The synthesis of SD-2301 is outlined in scheme 1 (Supplementary Fig. 1). It began with a known compound, **1**, which was converted into compound **2** through a two-step process. First, compound **1** was reacted with hept-6-ynoic acid to form an amide, which was then saponified using LiOH in aqueous media to yield acid intermediate **2** in 65% overall yield. Azide **6** was synthesized in 80% yield from commercially available amine **5** using a previously reported method. A click reaction between alkyne acid **2** and azide **6**, with sodium ascorbate and $CuSO_4$, resulted in acid intermediate **3** in 78% yield. Amine **7** was prepared from Boc-L-glutamine through a two-step procedure. Initially, Boc-L-glutamine was coupled with substituted benzyl amine in the presence of HATU (hexafluorophosphate azabenzotriazole tetramethyl uronium) and DIPEA (*N*,*N*-diisopropylethylamine) in DMF (*N*,*N*-dimethylformamide) to form a Boc-protected amide, which was then Boc-deprotected using 4 (N) HCl in DCM to give amine **7** in 70% yield over two steps. The coupling of acid **3** with amine **7** in the presence of HATU and DIPEA in DMF produced a Boc-protected intermediate. This intermediate was then Boc-deprotected using 4 (N) HCl in dioxane to yield amine intermediate **4** in 75% yield over two steps. Finally, compound **4** was converted into SD-2301 in 86% yield through an amide formation reaction with literature known intermediate **8**, using HOBt and DIPEA in DMF.

The purity of SD-2301 was confirmed by ultra-performance liquid chromatography (UPLC) to be >99%. UPLC–MS (ESI) *m*/*z*: calculated, 683.7 for $C_{64}H_{80}N_{13}O_{15}PS_2$ $[M + 2H]^+/2$; found, 684.09 (Supplementary Fig. 2). Proton nuclear magnetic resonance (^{1}H-NMR) and carbon nuclear magnetic resonance (^{13}C-NMR) spectroscopies were performed on Bruker Advance 400 NMR spectrometers, and chemical shifts are reported in parts per million (ppm) relative to an internal standard (Supplementary Figs. 3 and 4).

In vivo mouse experiments

Animal studies were approved by the Institutional Animal Care and Use Committee at the University of Michigan. All mice were maintained under specific pathogen-free housing (about 22 °C with approximately 40% humidity) on a 12-h dark:12-h light cycle. The following mice (at 6–8 weeks of age) (The Jackson laboratory) were used for this study: C57BL/6J, BALB/cJ, NOD-scid IL2Rγ null (NSG), Rag1tm1Mom (*Rag1*$^{-/-}$), C57BL/6-Tg(TcraTcrb)1100Mjb/J (OT-I), B6.129S(C)-Batf3tm1Kmm/J (*Batf3*$^{-/-}$), B6.129S(Cg)-*Stat1*tm1Dlv/J (*Stat1*$^{-/-}$), B6(129S4)-Xcr1tm1.1(cre) Kmm/J (*Xcr1*^{cre}), B6.129S1-*Stat3*tm1Xyfu/J (*Stat3*$^{fl/fl}$) mice and CD-1 mice were obtained from Charles River Laboratories. *Stat5b*$^{-/-}$ C57BL/6J mice were from the National Institutes of Health (Warren Leonard). *Stat3*$^{fl/fl}$ mice were crossed with *Xcr1*^{cre} mice to obtain specific STAT3 deficiency in DC1s (*Stat3*$^{-/-}$ mice). In-house littermates were used in the control arm when specific mouse strains were generated in-house.

MC38 (2×10^6), CT26 (10^5), EMT6 (10^5), B16F10 (2×10^5) and LLC (2×10^5) cells were injected subcutaneously into syngeneic mice. Luciferase-expressing ID8 cells (2×10^6) were injected into the peritoneal cavity of female mice. Luciferase-expressing 4T1 cells (10^5) were injected into female mouse mammary fat pad. From day 5–7, SD-36 (low doses: 10 or 20 mg kg^{-1}; high dose: 100 mg kg^{-1}) or SD-2301 (5 mg kg^{-1}) was administered intravenously every 3 days. In 4T1 tumour metastasis model, treatment with SD-36 (20 mg kg^{-1}) started on day 14, followed by every 3 days. In some cases, peritoneal tumour-bearing mice were similarly treated with SD-36 (20 mg kg^{-1}) or SD-2301 (5 mg kg^{-1}) or were injected intraperitoneally with FLLL32 (30 mg kg^{-1}) for 24 h. For the ICB experiments, PD-L1 monoclonal antibody or isotype antibody (BioXcell, 200 μg) were administrated intraperitoneally into tumour-bearing mice, starting on day 3, then repeated this treatment every 3 days. For DC1 transfusion experiments, bone marrow-derived cDC1s (2×10^6) were sorted and injected intravenously into tumour-bearing *Batf3*$^{-/-}$ mice on day −2 and day 8. SD-36 (20 mg kg^{-1}) was administered intravenously every three days, starting on day 5. Tumour inoculation time was considered day 0. Tumour cells were inoculated into age-, sex- and source-matched mice. Tumour size was measured using calipers with a Vernier scale and calculated as previously[46].

To evaluate tolerability and toxicity, tumour-bearing C57BL/6J mice received intravenous injections of SD-2301 (5 mg kg^{-1}) every 3 days for 18 days, with body weights were monitored throughout.

For pharmacokinetic evaluation, female CD-1 mice were administered a single intravenous dose of SD-2301 at 5 mg kg^{-1} with 25% of PCP as the dosing vehicle. Then, 250–300 μl blood samples were collected from 5 min to 24 h. Following centrifugation at 15,000 rpm for 10 min, at least 100 μl of plasma was collected. All samples were analysed by the Pharmacokinetic and Mass Spectrometry core at the University of Michigan. Compound concentrations in plasma were determined using a validated LC-MS/MS method with an internal control. Chromatographic separation was achieved with a Waters XBridge-C18 column (5 cm × 2.1 mm, 3.5 μm) on a Shimadzu HPLC system. Detection was performed on an AB Sciex QTrap 5500 mass spectrometer in positive-ion MRM mode. The mobile phases were 0.1% formic acid in water (A) and in acetonitrile (B). The gradient for B was: 10% (0–0.3 min), increased to 95% at 0.7 min, held for 2.3 min, and returned to 10% for a 2-min re-equilibration. Flow rate was 0.4 ml min^{-1}. Pharmacokinetic parameters were calculated using noncompartmental methods in WinNonlin v.3.2 (Pharsight).

Human studies

All clinical records used in this study were acquired and used with the approval of Institutional Review Boards. Patients (cohort 1) who underwent ICB therapy were recruited from the University of Michigan Hospital, Ann Arbor, MI, USA. Inclusion in the analysis applied to those who were enroled in the Michigan Center for Translational Pathology's (MCTP) continuous comprehensive clinical sequencing programme[39,47–49], MI-Oncoseq, and who possessed sequenced libraries of pre-treatment tumours. From the initiation of therapy, overall survival times were measured. Treatment responses were determined according to RECIST1.1 criteria[50] and imRECIST[51]. Integrative clinical sequencing was conducted using standard protocols approved for use in MCTP's Clinical Laboratory Improvement Amendments-compliant sequencing laboratory, as previously described[47,48,52]. After purification with the AllPrep DNA/RNA/miRNA kit (Qiagen), total RNA was sequenced using the exome-capture transcriptome platform on an Illumina HiSeq 2000 or HiSeq 2500 in paired-end mode. Quality control, alignment, and expression quantification was executed through the standard clinical RNA-seq pipeline, CRISP[53]. Read count tables were then normalized into fragments per kilobase million (FPKM) then transcripts per million (TPM) using the edgeR 4.2.2 package[54]. Gene scores in RNA-seq data were generated using the rank-based inverse normal transformation (INT) as demonstrated previously[55]. The CTL score and DC1 maturation score were generated using the following respective gene sets: (*CD8A*, *CXCL10*, *CXCL9*, *GZMA*, *GZMB*, *PRF1*, *IFNG* and *TBX21*) and (*CD40*, *CD80*, *CD86*, *HLA-DQA1*, *XCR1*, *CLEC9A*, *IL12A*, *IL12B*, *HLA-DRA* and *IDO1*). STAT5/STAT3 expression was calculated as the ratio of combined TPM of *STAT5A* and *STAT5B* (*STAT5AB*) to *STAT3* TPM for all patients (Extended Data Table 1). Stratification was performed at the median *STAT5AB*/*STAT3* TPM ratio and at the median DC1 maturation score. This was performed for cohort 2 (Extended Data Table 2) in each dataset, before combining group-wise. STAT5 pathway INT score was calculated using the GM-CSF reactome gene set (R-HSA-512988). STAT5 pathway/STAT3 was calculated by dividing the INT score by the *STAT3* TPM in each respective sample, this value was stratified by the median.

The single-cell RNA-seq analysis of TNBC (cohort 3) (dataset GSE169246) was conducted in R using Seurat (v.4.3.0), ssGSEA, and standard data wrangling and plotting packages. All analyses were carried out after subsetting the data for immunotherapy treatment. DCs were extracted based on the original authors' annotations. Only cells

expressing 200 or more genes in at least 3 cells were included in the analysis, and cells with mitochondrial reads greater than 10% were excluded. The STAT5 signalling score for each cell was calculated by applying the GM-CSF reactome gene set (R-HSA-512988) as input to the enrichIt function from the escape (v.2.0.0) package, which implements ssGSEA. Similarly, the STAT3 signalling score was determined using the same approach. The genes used for the IL-10-driven STAT3 signalling score were obtained from previously reported gene orthologues in murine DCs[56]. This gene set comprised: *RAP1GAP*, *CAMKK1*, *CASR*, *KIF1A*, *HPCAL4*, *DRAM1*, *RAMP2*, *MT2A*, *IGFBP6*, *GATA3*, *CXCR5*, *GDA*, *FAM65C* (also known as *RIPOR3*), *PLET1*, *SOCS3*, *MUC1* and *GBP5*. The DC maturation score was computed using the same method with genes canonically associated with DC maturation, including *CD40*, *CD80*, *CD83*, *CD86*, *LAMP3*, *CCL19*, *IL12A*, *IL12B*, *CCL5*, *CCL22*, *CXCL9*, *CXCL10*, *NFKB1*, *NFKB2*, *NFKBIA*, *NFKBIB*, *FSCN1* and *CCR7*. The binary division of high and low STAT3 signalling scores was determined by visually identifying two distinct clusters. The monocyte-DCs versus conventional DC distinction was determined through a combination of iterative clustering and expression of CD14. The Wilcoxon signed-rank test was used to compare the ssGSEA scores using the stat_compare_means function from the ggpubr (v.0.6.0) package.

For the in vitro human ICB study, lin$^-$CD45$^+$CD11c$^+$MHCII$^+$ DCs were enriched and sorted from fresh cancer tissues of patients with high grade serous ovarian carcinoma. DCs (10^6 per ml) were pretreated with SD-36 (1 μM), washed, and co-cultured with normal peripheral blood T cells (2×10^6 per ml) in the presence of anti-human PD-L1 (10 μg ml^{-1}), anti-CD3 (2 μg ml^{-1}), and anti-CD28 (1 μg ml^{-1}) for 3 days. T cell cytokine profile was analysed by FACS. For detecting the effect of SD-2301 on STAT members in human immune cells in vitro, normal human peripheral blood mononuclear cells (PBMCs) were treated with SD-2301 for 14 h, followed by immunoblotting to analyse STAT protein levels. Normal human immune cells were collected from commercial buffy coats (Carter BloodCare).

Bulk RNA-seq analysis in mouse DCs

Data processing. cDC1s were purified from BMDCs as described above. The RNA was isolated by column purification (Qiagen, 217048) with DNase treatment. The RNA-seq was conducted by BGI Genomics. Bulk RNA-seq analysis was performed using the edgeR (v.4.2.2) and limma (v.3.60.6) package workflows. Preliminary quality control measures were performed including the filtering of lowly expressed genes, and the calculation and assessment of library sizes across samples. The raw counts were then transformed to log counts per million (CPM) values.

Differential expression analysis. A design matrix was created containing cell population information (*Stat3*$^{-/-}$ versus *Stat3*$^{+/+}$) and then contrasts for pairwise comparisons between *Stat3*$^{-/-}$ and *Stat3*$^{+/+}$ were determined in limma using the makeContrasts function. As an additional normalization measure, removal of heteroscedasticity from the normalized counts data was achieved using the voom function. To identify differentially expressed genes, the mean-variance relationship of the normalized counts was assessed and then the normalized data were modelled as a linear combination of factors and covariates. The cutoff for the *P* value was $P = 0.05$. Differential expression analysis was performed on non-treated *Stat3*$^{-/-}$ versus *Stat3*$^{+/+}$ cDC1s and LPS-treated *Stat3*$^{-/-}$ versus *Stat3*$^{+/+}$ cDC1s, respectively.

Gene signature analysis. To assess the DC maturation signature, the log fold change and *P* values of DC maturation genes reported in the literature including (*Cd40*, *Cd80*, *Cd83*, *Cd86*, *Ido1*, *Irf7*, *Tnfsf8*, *H2-Aa*, *H2-ab1*, *Tlr4*, *Il12b*, *Il12rb1*, *Il12rb2* and *Cxcl9*) was observed from the differential expression analysis results. To assess the significantly upregulated DC maturation pathways, gene set enrichment analysis (GSEA) was performed on the *Stat3*$^{-/-}$ versus *Stat3*$^{+/+}$ differentially expressed genes in R using the gseGO function. To assess the significantly upregulated DC activation pathways in the DCs treated with LPS, GSEA was performed on the LPS-treated *Stat3*$^{-/-}$ versus *Stat3*$^{+/+}$ differentially expressed genes in R using the gseGO function.

Data visualization. The *z*-score of the normalized counts were computed and plotted as a heat map using GraphPad Prism 10.2.2. DC maturation genes were selected from the differential expression analysis results and the log fold change and *P* values were plotted using GraphPad Prism 10.2.2. The GSEA plots were generated in R using the gseaplot function. The GSEA dot plot was generated by plotting key pathways from the GSEA results using the dotplot function from clusterProfiler 4.9.2 package. The volcano plot was generated by first performing differential expression analysis of LPS-treated *Stat3*$^{-/-}$ versus *Stat3*$^{+/+}$ cDC1s and plotting log fold changes and *P* values of genes from the STAT5 pathway curated in the Hallmark pathway Molecular Signature Database (MSigDB).

Chromatin immunoprecipitation

Chromatin immunoprecipitation was performed using the SimpleChIP Enzymatic Chromatin IP Kit (Cell Signaling Technology, 9003s). Sheared chromatin was then immunoprecipitated with STAT5 (Cell Signaling Technology, 94205s) and IgG (Cell Signaling Technology, 2729) antibodies. SYBR green master mix (Applied Biosystems) was used to measure amplification of DNA using QuantStudio 3 Fast Real-Time PCR system (Applied Biosystems). The promoters of gene were quantified using the specific primers (Extended Data Table 3). After normalization to the Input DNA, the amount of output DNA of each target protein was calculated by subtracting that of the IgG control.

Flow cytometry analysis

Single-cell suspensions were prepared from fresh mouse tumour tissues or spleen, and lymphocytes were enriched by density gradient centrifugation. To assess intracellular cytokine production, cells were cultured for 4 h in the presence of phorbol myristate acetate (5 ng ml^{-1}; Sigma-Aldrich), ionomycin (500 ng ml^{-1}; Sigma-Aldrich) and brefeldin A (1: 1000, BD Biosciences). Cells were fixed and permeabilized with the Transcription factor staining buffer set (Invitrogen, 00-5523-00). Cellular phenotypes were assessed multi-parameter flow cytometry panels. Data were acquired on a BD LSRFortessa. Antibodies against the following mouse antigens were used: CD45 (30-F11, HI30), CD90 (53-2.1, 30-H12), CD3 (17A2), CD45R/B220 (RA3-6B2), CD4 (RM4-5, GK1.5), CD8 (53−6.7), IFNγ (XMG1.2), granzyme B (GB11), IL-2 (JES6-5H4), Ki-67 (B56), I-A/I-E (M5/114.15.2), CD80 (16-10A1), CD86 (GL1), H-2Kb (AF6-88.5.5.3), H-2 (M1/42), XCR1 (ZET), TNF (MP6-XT22), CD11c (HL3), phospho-Tyr694-STAT5 (SRBCZX), phospho-Tyr705-STAT3 (13A3-1). Additionally, antibodies against the following human antigens were used: CD8 (RPA-T8), IFNγ (B27) and TNF (MAb11). The strategies for DC gating and in vitro cultures and tissues are shown in Extended Data Figs. 2c and 3e, respectively. The strategy for T cell gating is presented in Extended Data Fig. 3k.

Statistics and reproducibility

Sample sizes were determined based on previously published studies to ensure appropriate statistical power. In vitro experiments were performed in at least two independent replicates. For in vivo studies, each group consisted of a minimum of five mice, which was considered sufficient to detect meaningful biological differences with good reproducibility, and mice were randomized into treatment groups at the start of the experiment. Experiments were not performed in a blinded manner, as knowledge of the treatment groups were necessary to carry out the study. *t*-tests were used to assess differences between two independent experimental groups, and one-way analysis of variance (ANOVA) was used to compare three or more groups. Two-way ANOVA was applied to compare tumour growth curves. Data are presented as mean ± s.e.m., and statistical significance was defined as

$P < 0.05$ for all tests. All statistical analyses related to these experiments were performed using GraphPad Prism software v.10.2.2.

Kaplan–Meier analysis was conducted to estimate overall survival, with differences between groups assessed using log-rank tests. Cox proportional hazards models were used for multivariate survival analysis. Pearson's correlation coefficient was applied to evaluate linear correlations between variables, and the Wilcoxon rank-sum test was performed to assess group differences. All *P* values are two-sided and not adjusted for multiple comparisons. The statistical analyses were conducted using R packages.

Ethics oversight

All human studies were conducted under the oversight and approval of the Institutional Review Board at the University of Michigan Medical School.

Reporting summary

Further information on research design is available in the Nature Portfolio Reporting Summary linked to this article.

Data availability

Clinical sequencing data are publicly available with raw data available upon request from dbGaP phs000673.v5.p1 (refs. 39,47). RNA-seq data that were newly generated in this study for in vitro analysis have been deposited at the Gene Expression Omnibus (GEO) at NCBI under accession GSE289764. Single-cell RNA-seq data that support the findings of this study were downloaded from GEO accession GSE169246. The two original melanoma RNA-seq datasets were deposited in the European Nucleotide Archive (ENA) under accession PRJEB23709 and in dbGaP under accession phs000452.v2.p1. The processed data for these two melanoma datasets can be found at https://ngdc.cncb.ac.cn/icb/resources. All materials are available from the corresponding authors upon reasonable request. Source data are provided with this paper.

46. Wang, D. et al. Controllable synthesis of dual-MOFs nanostructures for pH-responsive artemisinin delivery, magnetic resonance and optical dual-model imaging-guided chemo/photothermal combinational cancer therapy. *Biomaterials* **100**, 27–40 (2016).
47. Robinson, D. R. et al. Integrative clinical genomics of metastatic cancer. *Nature* **548**, 297–303 (2017).
48. Wu, Y. M. et al. Inactivation of CDK12 delineates a distinct immunogenic class of advanced prostate cancer. *Cell* **173**, 1770–1782 (2018).
49. Wang, W. et al. CD8$^+$ T cells regulate tumour ferroptosis during cancer immunotherapy. *Nature* **569**, 270–274 (2019).
50. Watanabe, H. et al. New response evaluation criteria in solid tumours-revised RECIST guideline (version 1.1). *Gan To Kagaku Ryoho* **36**, 2495–2501 (2009).
51. Hodi, F. S. et al. Immune-modified Response Evaluation Criteria In Solid Tumors (imRECIST): refining guidelines to assess the clinical benefit of cancer immunotherapy. *J. Clin. Oncol.* **36**, 850–858 (2018).
52. Parolia, A. et al. Distinct structural classes of activating FOXA1 alterations in advanced prostate cancer. *Nature* **571**, 413–418 (2019).
53. Cieslik, M. et al. The use of exome capture RNA-seq for highly degraded RNA with application to clinical cancer sequencing. *Genome Res.* **25**, 1372–1381 (2015).
54. Robinson, M. D., McCarthy, D. J. & Smyth, G. K. edgeR: a Bioconductor package for differential expression analysis of digital gene expression data. *Bioinformatics* **26**, 139–140 (2010).
55. Yang, J. et al. FTO genotype is associated with phenotypic variability of body mass index. *Nature* **490**, 267–272 (2012).
56. Chrisikos, T. T. et al. STAT3 inhibits autocrine IFN signaling in type i conventional dendritic cells. *J. Immunol.* **209**, 1286–1299 (2022).

Acknowledgements The authors thank J. Deng for providing *Stat1*$^{-/-}$ C57BL/6J mice (originally from The Jackson Laboratory); M. Wang, B. Wen and D. Sun for the pharmacokinetics study; and our laboratory members for their intellectual input. This work was supported in part by research grants from the Breast Cancer Research Foundation, NIH/NCI R01 grants (CA217648, CA123088, CA099985, CA193136, CA152470 and CA244509), and the NIH/NCI through the University of Michigan Rogel Cancer Center Grant (CA46592). J.-X.L. and W.J.L. are supported by the Division of Intramural Research, the National Heart, Lung and Blood Institute, the National Institutes of Health.

Author contributions J.Z. conceived the study, designed experiments, conducted experiments and wrote and revised the manuscript. K.T. performed human bioinformatic analyses and wrote and revised the manuscript. H.Z. developed SD-36. L.B. developed SD-36 and SD-2301 and conducted in vitro human PBMC studies with SD-2301. R.K.A. developed SD-2301. D.M. assisted with in vivo experiments and supervised the use of SD-36 and SD-2301. H.M. provided assistance with in vivo experiments. Y.W. conducted the pharmacokinetics study. M.P. performed mouse bioinformatic analyses. J.E.C. assisted with human bioinformatic analyses. L.V. performed flow cytometry sorting of samples. P.L. designed ChIP–qPCR primers. J.Y. assisted in preparing single-cell suspensions from mouse tumour tissues. H.L. assisted with antigen presentation assays. L.J. assisted with the identification of *Stat3*$^{+/+}$ and *Stat3*$^{-/-}$ mice. S. Wei identified and generated *Stat3*$^{+/+}$ and *Stat3*$^{-/-}$ mice and guided the protocol for experimental animals. X.G. assisted with phospho-kinase array. S.G. generated *Stat3*$^{+/+}$ and *Stat3*$^{-/-}$ mice. A.P. supervised bioinformatic analyses. M.C. assisted in acquiring human tumour samples and provided bioinformatic support. I.K. conducted in vitro human studies, assisted with the analysis of flow cytometry data, provided scientific input, engaged in discussions, revised the manuscript and supervised the study. M.D.G. contributed to the acquisition of human tumour samples and oversaw bioinformatic support. J.-X.L. provided *Stat5b*$^{-/-}$ mice. A.M.C. had a role in acquiring of clinical samples and supervised bioinformatic support. W.J.L. provided *Stat5b*$^{-/-}$ mice, provided scientific input, participated in discussions and revised the manuscript. S. Wang conceived the study, developed SD-36 and SD-2301, designed experiments, provided scientific input, participated in discussions, revised the manuscript, supervised the study and acquired funding. W.Z. conceived the study, designed experiments, composed the manuscript, provided scientific input, participated in discussions, wrote and revised the manuscript, supervised the study and acquired funding.

Competing interests W.Z. serves as a scientific advisor or consultant for Cstone, Hanchor Bio and NextCure and was a consultant for Oncopia. S. Wang was a co-founder and a paid consultant for Oncopia Therapeutics and owned equity in Oncopia, which was acquired by Roivant Sciences and Proteovant Therapeutics. S. Wang was a paid consultant for Proteovant Therapeutics and Roivant Sciences and owned stock in Roivant Sciences. S. Wang was the principal investigator for a research contract between Oncopia/Proteovant and the University of Michigan. S. Wang is a co-founder, paid consultant, and member of the board of directors of Ascentage Pharma Group International and owns stock in Ascentage. A.M.C. was a co-founder and a paid consultant for Oncopia and owned equity in Oncopia and was a paid consultant for Proteovant Therapeutics. The University of Michigan owned stock in Oncopia and Ascentage. The University of Michigan has filed multiple patents on STAT3 degraders, which have been licensed by Oncopia/Proteovant (now SK Life Science Labs) for clinical development. S. Wang, H.Z., L.B., R.K.A., D.M. and H.M. are inventors on SD-36 and/or SD-2301 and have received royalty payments from the University of Michigan. All other authors declare no competing interests.

Additional information

Supplementary information The online version contains supplementary material available at https://doi.org/10.1038/s41586-025-09000-3.

Correspondence and requests for materials should be addressed to Shaomeng Wang or Weiping Zou.

Peer review information *Nature* thanks David Frank, Ignacio Melero and the other, anonymous, reviewer(s) for their contribution to the peer review of this work.

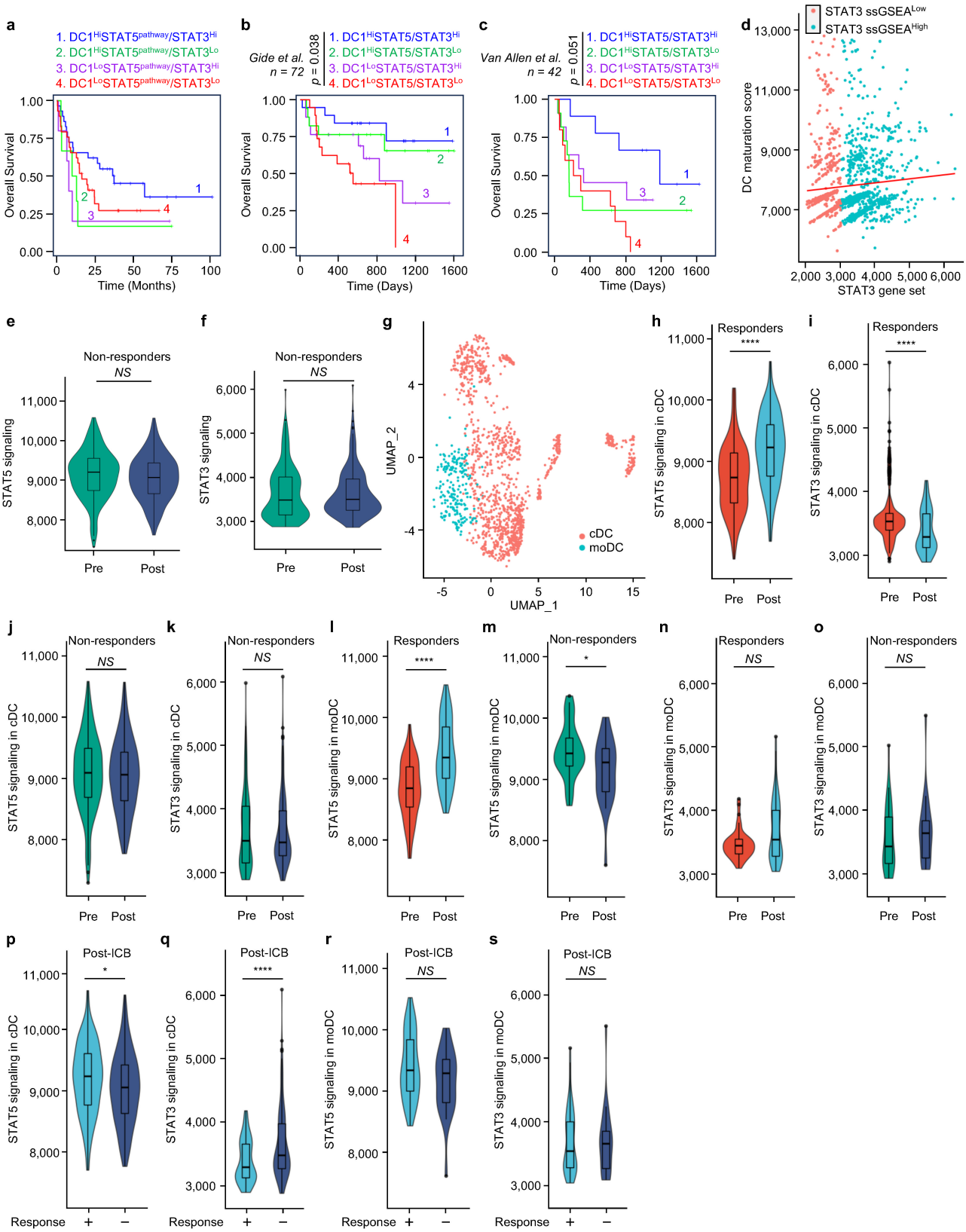

Extended Data Fig. 1 | See next page for caption.

Extended Data Fig. 1 | Role of DC STAT5 and STAT3 in ICB. a. The Kaplan Meier (KM) survival curve was plotted to visualize the difference in survival probability between patient stratifications. Cohort 1 patients with ICB unresponsive tumors (sarcoma, lymphoma, prostate cancer, and others) were excluded for analysis. n = 69, $p = 0.0374$, the CoxPH model calculates the effect of the STAT5 pathway/*STAT3* DC maturation (high/high group) on survival outcome relative to STAT5 pathway/*STAT3* DC maturation (high/low group) when tumor type is controlled. **b**-**c**. KM curves of OS in melanoma patients (cohort 2) treated with ICB, by low or high DC score and the ratio of *STAT5* versus *STAT3* ($DC1^{Hi}STAT5/STAT3^{Hi}$, $DC^{Hi}STAT5/STAT3^{Lo}$, $DC^{Lo}STAT5/STAT3^{Hi}$, $DC^{Lo}STAT5/STAT3^{Lo}$). n = 72 (**b**), n = 42 (**c**), $p = 0.038$ (**b**), $p = 0.051$ (**c**) by log-rank test. **d**. High and low STAT3 gene signaling scores in patients with TNBC (cohort 3). Based on the STAT3 ssGSEA score, two distinct clusters were resolved. **e**-**f**. STAT5 and STAT3 gene signatures in DCs in non-responders (cohort 3). STAT5 (**e**) and STAT3 (**f**) gene signatures were analyzed in DCs in the post-ICB samples of non-responders compared to their pre-ICB samples. NS, not significant, Wilcoxon Rank-sum test. **g**. UMAP representations were used to identify different DC subtypes from the integrated scRNA-seq datasets of TNBC (cohort 3). The cells were then color-coded according to their respective DC subtypes. **h**-**s**. STAT5 and STAT3 gene signatures in cDCs and moDCs during ICB treatment (cohort 3). STAT5 (**h**, **j**, **l**, **m**, **p**, and **r**) and STAT3 (**i**, **k**, **n**, **o**, **q**, and **s**) gene signatures in cDCs and moDCs were compared between responders and non-responders after ICB treatment in TNBC. $^{*}p = 0.036$ (**m**), $^{*}p = 0.034$ (**p**), $^{****}p < 0.0001$ (**h**, **i**, **l**, **q**), Wilcoxon Rank-sum test. the central line represents the median. The lower and upper hinges of the box correspond to the 25^{th} and 75^{th} percentiles. The whiskers extend to the smallest and largest values no further than 1.5 * IQR from the hinges. Outliers are plotted as individual points.

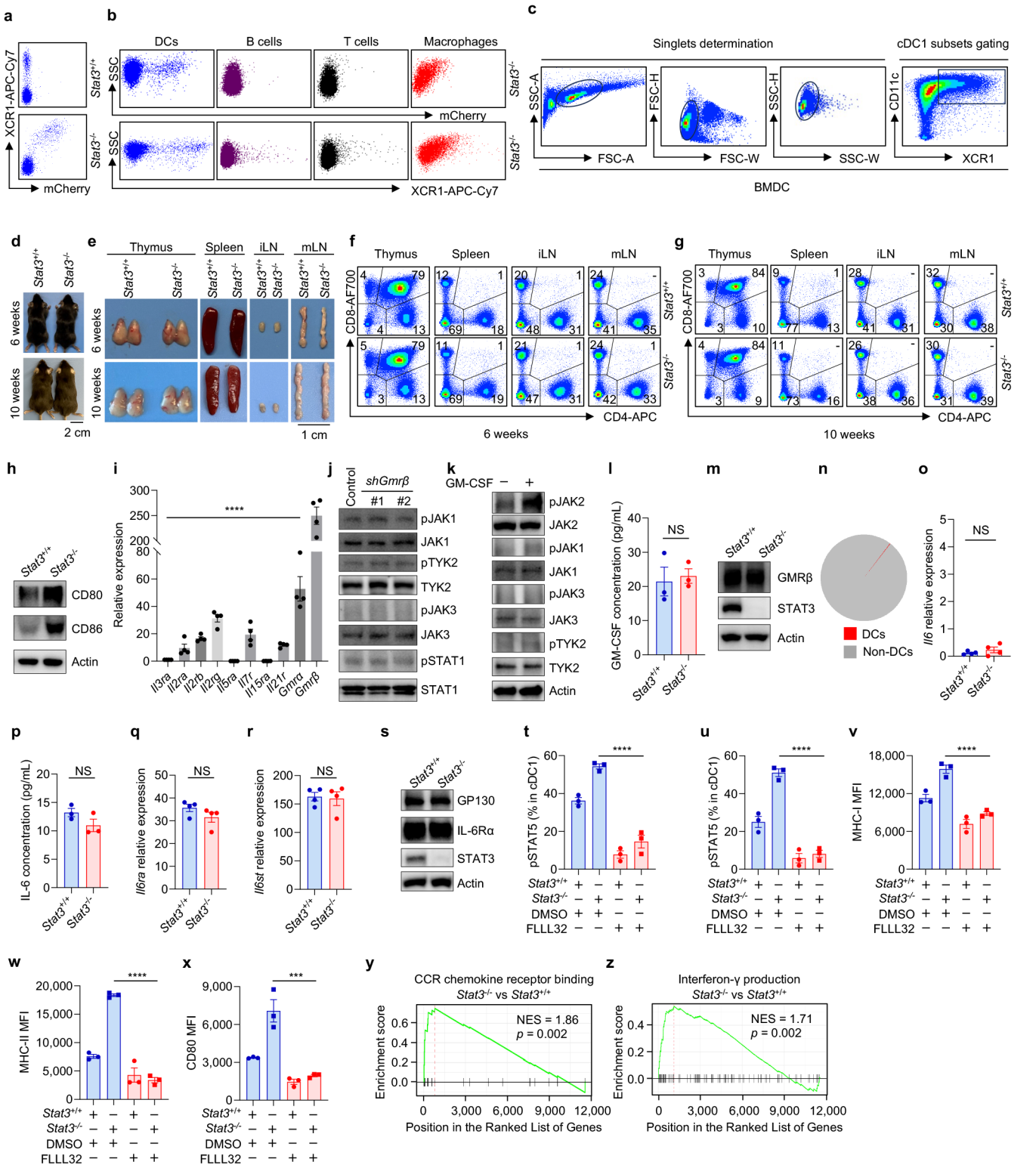

Extended Data Fig. 2 | See next page for caption.

Extended Data Fig. 2 | STAT3 restrains STAT5-driven DC function. a-b. *Xcr1* Cre knock-in mice express an mCherry fluorescent protein under the control of the Xcr1 promoter in cDC1s. mCherry expression and XCR1-APC-Cy7 staining in DCs from *Stat3*$^{+/+}$ and *Stat3*$^{-/-}$ mice were analyzed by FACS (**a**). mCherry expression and XCR1-APC-Cy7 staining in DCs (CD11c), B cells (B220), T cells (CD3 and CD90), macrophages (F4/80) from *Stat3*$^{-/-}$ mice were analyzed by FACS (**b**). One of four mice is shown. **c**. Gating strategy for cDC1s (CD11c^{+}XCR1^{+}) in BMDCs. **d-g**. Phenotype of *Stat3*$^{-/-}$ mice. The representative images show mouse body size (**d**), lymphoid organs (**e**), and T cell subset distribution (**f-g**) in *Stat3*$^{+/+}$ and *Stat3*$^{-/-}$ mice. **h**. Western blotting shows CD80 and CD86 expression in *Stat3*$^{+/+}$ and *Stat3*$^{-/-}$ cDC1s. One of three experiments is shown. **i**. Real time qPCR shows the expression of cytokine receptor mRNAs in mouse cDC1s. mean ± SEM, n = 4, ****$p < 0.0001$, one-way ANOVA. **j**. Effect of GMRβ knockdown on the JAK-STAT signaling pathway. JAWSII cells were transfected with shRNAs against *Gmrβ* or control shRNA and cultured with GM-CSF. Cell lysates were subjected to analysis by immunoblots. One of three experiments is shown. **k**. Effect of GM-CSF on JAWSII cells. The immunoblots show the expression levels of JAK family members in JAWSII cells. One of three experiments is shown. **l-m**. Effect of STAT3 deletion on GM-CSF and GMRβ expression in cDC1s. GM-CSF was detected by ELISA in culture supernatants in *Stat3*$^{+/+}$ and *Stat3*$^{-/-}$ cDC1s on day 5 (**l**). n = 3, NS, not significant, unpaired two-tailed t-test. GMRβ was determined by Western blotting (**m**). One of three experiments is shown. **n**. The fractions of IL-6^{+} DCs (in red) and non-DCs are depicted in the TNBC patient dataset[30]. **o**. RNA-seq analysis (from Fig. 2n) shows the expression of *Il6* by TPM (Transcripts Per Million) in mouse *Stat3*$^{+/+}$ and *Stat3*$^{-/-}$ cDC1s. n = 4, NS, not significant, unpaired two-tailed t-test. **p**. Effect of STAT3 deletion on IL-6 expression in cDC1s. IL-6 was detected by ELISA in culture supernatants in *Stat3*$^{+/+}$ and *Stat3*$^{-/-}$ cDC1s on day 4. n = 3, NS, not significant, unpaired two-tailed t-test. **q-r**. RNA-seq analysis (from Fig. 2n) shows the expression of IL-6 receptors (*Il6ra*, *Il6st*) by TPM (Transcripts Per Million) in mouse *Stat3*$^{+/+}$ and *Stat3*$^{-/-}$ cDC1s. n = 4, NS, not significant, unpaired two-tailed t-test. **s**. Western blot shows expression of IL-6Rα and GP130 in *Stat3*$^{+/+}$ and *Stat3*$^{-/-}$ cDC1s. One of three experiments is shown. **t-x**. Effect of FLLL32 on STAT5 activation and DC maturation in vivo. *Stat3*$^{+/+}$ and *Stat3*$^{-/-}$ mice bearing peritoneal B16F10 (**t**) and MC38 (**u-x**) tumors were treated with FLLL32 on day 9 for 24 h. FACS shows expression of pSTAT5 (**t**, **u**), MHC-I (**v**), MHC-II (**w**), and CD80 (**x**) in peritoneal cDC1s. MFI, mean fluorescence intensity. mean ± SEM, n = 3. ****$p < 0.0001$ (**t-w**), ***$p = 0.0001$ (**x**), one-way ANOVA. **y-z**. GSEA analysis reveals significant differences in the CCR chemokine receptor binding (**y**) and interferon gamma production (**z**) between *Stat3*$^{+/+}$ and *Stat3*$^{-/-}$ cDC1s. Source data contained unprocessed WB.

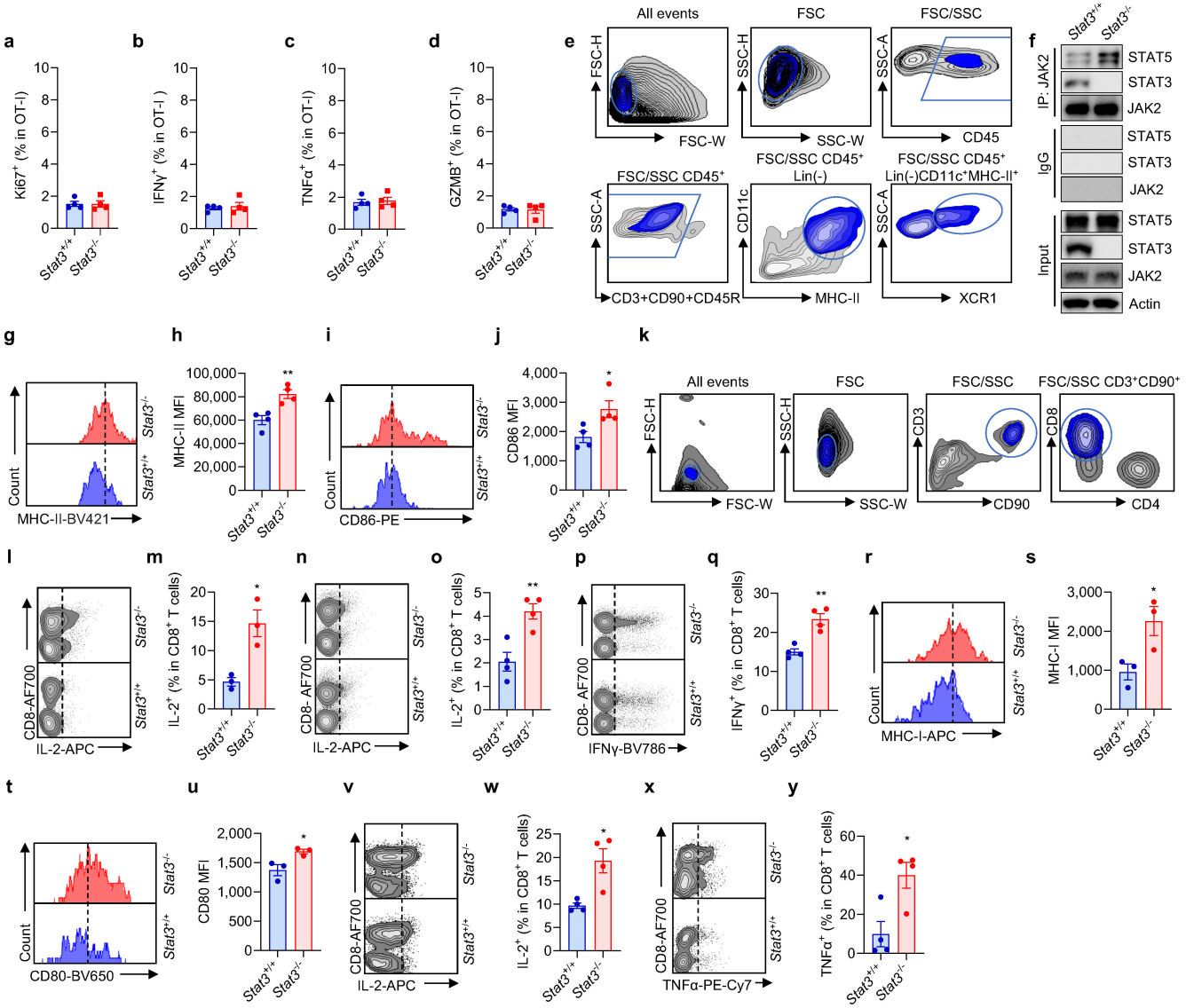

Extended Data Fig. 3 | STAT3 dampens DC1-mediated immunity. a-d. Effect of STAT3 deletion on DC-mediated T cell activation. OT-I cells were cultured with *Stat3*$^{+/+}$ or *Stat3*$^{-/-}$ cDC1s without loading SIINFEKL peptides. FACS shows the percentage of Ki67$^+$ (**a**), IFNγ$^+$ (**b**), TNFα$^+$ (**c**), and GZMB$^+$ (**d**) OT-I cells. **e.** Gating strategy for cDC1s (CD11c$^+$XCR1$^+$) in MC38 tumor bearing mouse model. **f.** Effect of STAT3 deficiency on the interaction between JAK2, STAT3, and STAT5 in DCs in vivo. Lin$^-$ CD11c$^+$XCR1$^+$ cDC1s were enriched and sorted from the TME in *Stat3*$^{+/+}$ and *Stat3*$^{-/-}$ mice bearing peritoneal MC38 tumors. Co-immunoprecipitation (IP) was performed with anti-JAK2 in DC lysates. One of two experiments with repeats is shown. **g-j.** MC38 tumors were inoculated into *Stat3*$^{+/+}$ and *Stat3*$^{-/-}$ mice. MHC-II (**g**, **h**), and CD86 (**i**, **j**) expression in cDC1 from MC38 tumor-draining lymph nodes (TDLNs) were analyzed by FACS. mean ± SEM, n = 4, $^{**}p = 0.0062$ (**h**), $^{*}p = 0.0335$ (**j**), unpaired two-tailed t-test. **k.** Gating strategy for CD8$^+$ T cells in MC38 tumor bearing mouse model. **l-q.** Effect of STAT3 deletion on MC38 tumor progression. FACS shows the percentages of MC38 tumor infiltrating IL-2$^+$CD8$^+$ T cells (**l**, **m**), and the percentages of TDLN IL-2$^+$ (**n**, **o**), and IFNγ$^+$ (**p**, **q**) CD8$^+$ T cells. For **l**, **n**, and **p**, one representative dot plot is shown in each panel. mean ± SEM, n = 3 (**m**), n = 4 (**o**, **q**), $^{*}p = 0.0141$ (**m**), $^{**}p = 0.006$ (**o**), $^{**}p = 0.0021$ (**q**), unpaired two-tailed t-test. **r-y.** Effect of STAT3 deletion on the phenotype of DCs and T cells in B16F10 bearing mice. FACS shows the expression of MHC-I (**r**, **s**) and CD80 (**t**, **u**) in tumor-infiltrating cDC1s, and the percentages of tumor infiltrating IL-2$^+$ (**v**, **w**) and TNFα$^+$ (**x**, **y**) CD8$^+$ T cells. For **r**, **t**, **v**, and **x**, one representative dot plot is shown in each panel. MFI, mean fluorescence intensity. mean ± SEM, n = 3 (**s**, **u**), n = 4 (**w**, **y**), $^{*}p = 0.038$ (**s**), $^{*}p = 0.0363$ (**u**), $^{*}p = 0.0109$ (**w**), $^{*}p = 0.0172$ (**y**), unpaired two-tailed t-test. Source data contained unprocessed WB.

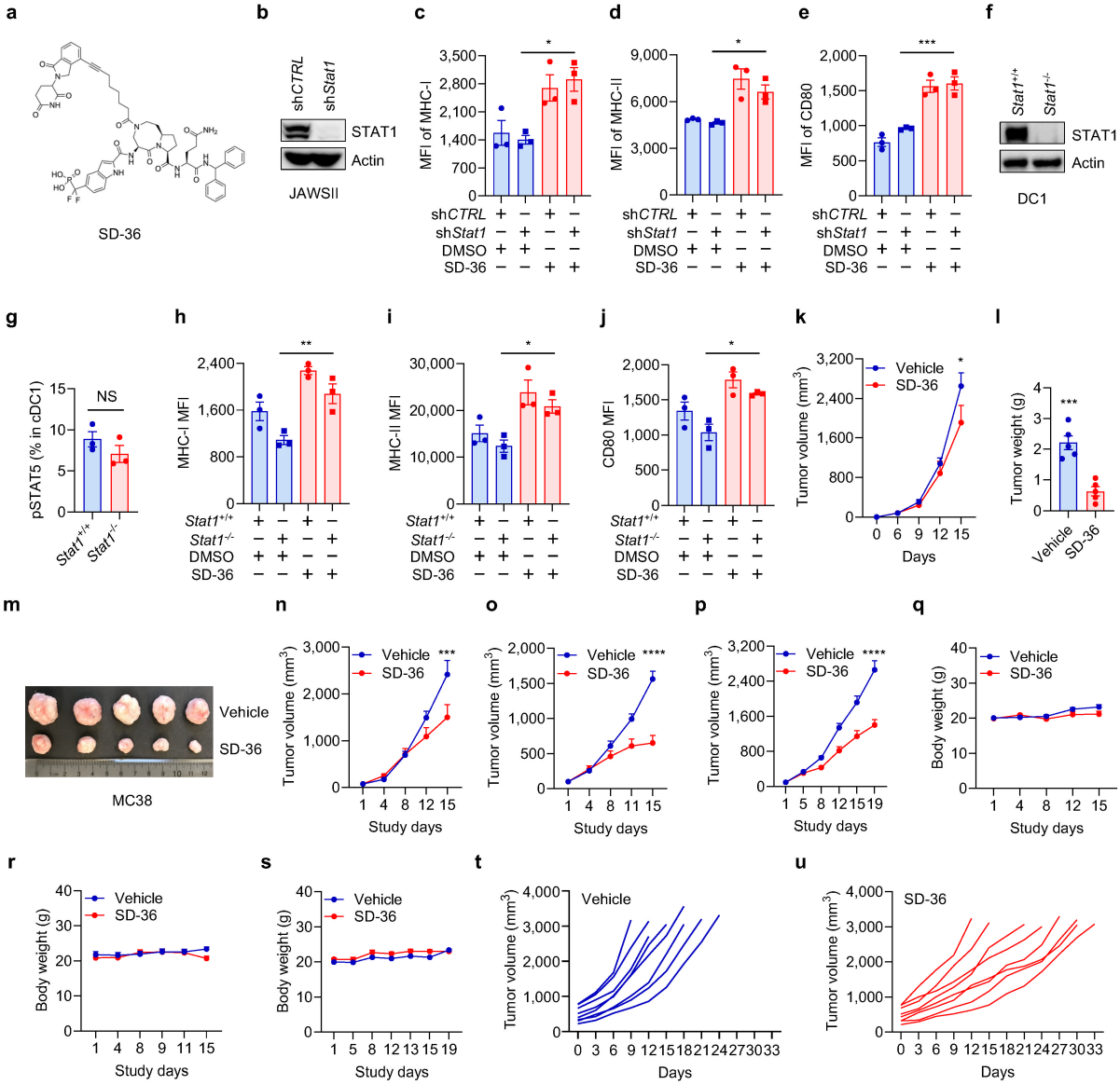

Extended Data Fig. 4 | STAT3 degrader treats advanced tumors. a. SD-36 structure is shown. **b**. Immunoblotting shows STAT1 in sh*Stat1* JAWSII cells. **c-e**. Effect of STAT1 on SD-36-regulated DC phenotype. FACS shows the expression of MHC-I (**c**), MHC-II (**d**), and CD80 (**e**) in sh*Stat1* JAWSII cells treated with SD-36. MFI, mean fluorescence intensity. means ± SEM, n = 3, *$p = 0.0117$ (**c**), *$p = 0.0195$ (**d**), ***$p = 0.0006$ (**e**), one-way ANOVA. **f**. Immunoblotting shows STAT1 in bone marrow derived DC1s from *Stat1*$^{+/+}$ and *Stat1*$^{-/-}$ mice. One of three experiments is shown. **g**. Effect of STAT1 on STAT5 activation in cDC1s. FACS shows the expression of pSTAT5 in bone marrow derived *Stat1*$^{+/+}$ and *Stat1*$^{-/-}$ cDC1s. n = 3, NS, not significant, unpaired two-tailed t-test. **h-j**. Effect of STAT1 on SD-36-regulated DC maturation. *Stat1*$^{+/+}$ and *Stat1*$^{-/-}$ DCs were treated with SD-36 for 12 h. FACS shows the expression of MHC-I (**h**), MHC-II (**i**), and CD80 (**j**) in cDC1s. MFI, mean fluorescence intensity. means ± SEM, n = 3, *$p = 0.0314$ (**i**), *$p = 0.0138$ (**j**), **$p = 0.0059$ (**h**), one-way ANOVA. **k**. Effect of SD-36 on B16F10 tumor progression. B16F10 tumor bearing C57/B6 mice were treated with 10 mg/kg SD-36. Tumor volumes were shown. mean ± SEM, n = 7, *$p = 0.0114$, two-way ANOVA. **l-m**. Effect of SD-36 on MC38 tumor progression. MC38 tumor bearing C57/B6 mice were treated with SD-36. Tumor weight (**l**) and image (**m**) were shown. mean ± SEM, n = 5, ***$p = 0.0004$, unpaired two-tailed t-test. **n-s**. Effect of SD-36 on tumor progression (**n-p**) and mouse body weights (**q-s**). Mice bearing B16F10 (**n**, **q**), CT26 (**o**, **r**), and EMT6 (**p**, **s**) were treated with SD-36 (100 mg/kg) three times a week when tumor volume reached 100 mm^3. Tumor volumes and mouse body weights were monitored. means ± SEM are shown, n = 8 (**n**, **q**), n = 10 (**o**, **p**, **r**, **s**), ***$p = 0.0005$ (**n**), ****$p < 0.0001$(**o**, **p**), two-way ANOVA. **t-u**. Effect of SD-36 on large tumor progression. Mice bearing CT26 tumors (500 mm^3/tumor) were treated with vehicle (**t**) or SD-36 (**u**). Tumor volumes were monitored. Source data contained unprocessed WB.

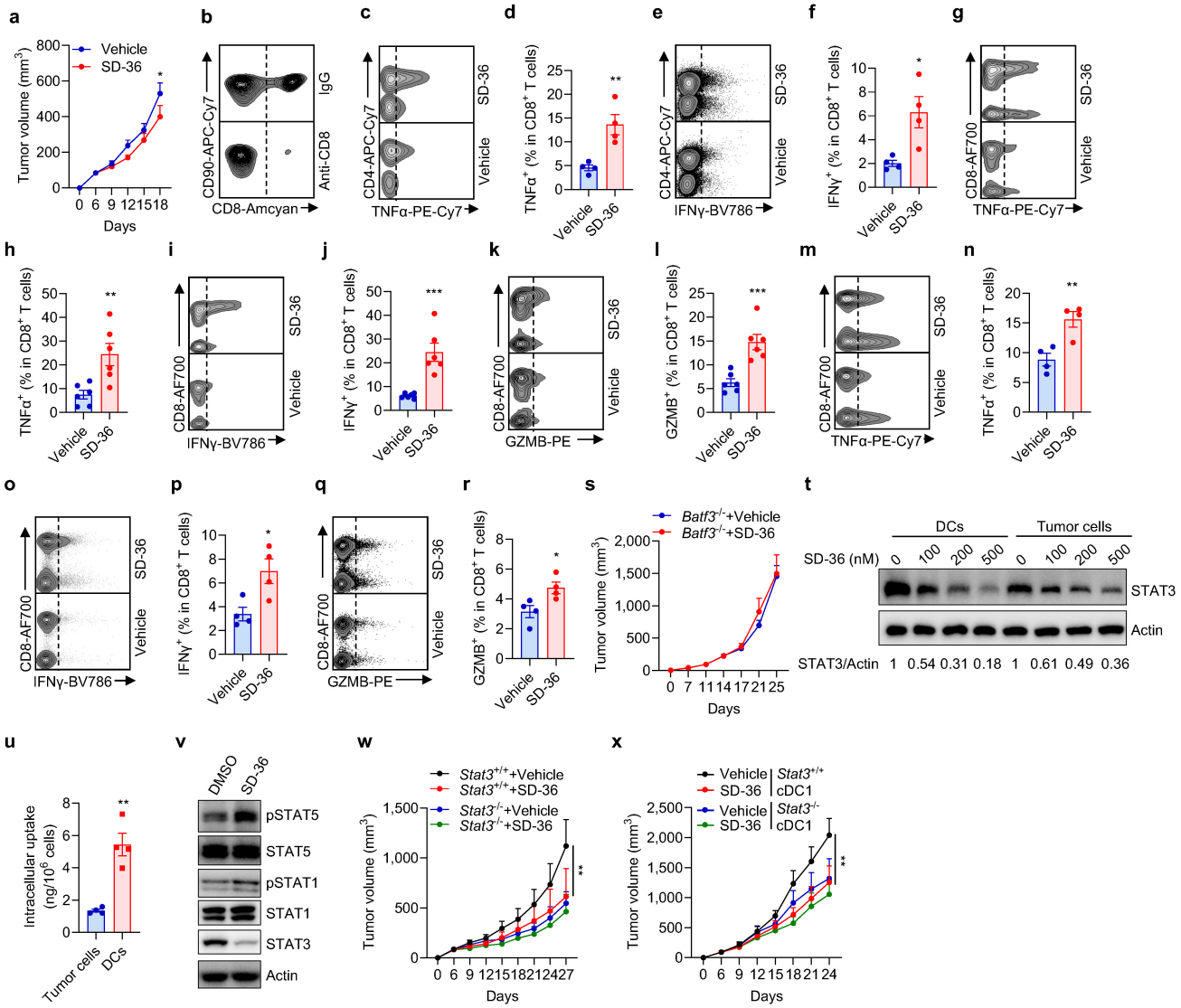

Extended Data Fig. 5 | STAT3 degradation in DCs boosts immunity. a. Effect of SD-36 on tumor growth in NSG mice. MC38 tumor-bearing NSG mice were treated with SD-36 (100 mg/kg) or vehicle. Tumor volume was monitored. mean ± SEM, *p = 0.0326, two-way ANOVA. **b.** Efficacy of anti-CD8 mAb in CD8$^+$ T cell depletion. MC38 bearing were treated with anti-CD8 mAb. FACS shows CD8$^+$ T cells in the tumor draining lymph node (TDLN). One of 5 is shown. **c-f.** Role of SD-36 in CD8$^+$ T cells in 4T1 tumor draining lymph nodes (TDLN). 4T1 tumor bearing mice were treated with SD-36. FACS shows the percentages of TDLN TNFα$^+$ (**c, d**), and IFNγ$^+$ (**e, f**) CD8$^+$ T cells. For **c**, **e**, one representative dot plot is shown in each panel. mean ± SEM, n = 4, *p = 0.0184 (**f**), **p = 0.0063 (**d**), unpaired two-tailed t-test. **g-r.** Role of SD-36 in CD8$^+$ T cells in LLC tumor bearing mice. FACS shows the percentages of TNFα$^+$ (**g**, **h**), IFNγ$^+$ (**i**, **j**), and GZMB$^+$ (**k**, **l**) CD8$^+$ T cells from tumors (**g-l**) and tumor-draining lymph nodes (**m-r**). For **g**, **i**, **k**, **m**, **o**, and **q**, one representative dot plot is shown in each panel. mean ± SEM, n = 6 (**h**, **j**, **l**), n = 4 (**n**, **p**, **r**), *p = 0.0224 (**p**), *p = 0.0294 (**r**), **p = 0.0072 (**h**), **p = 0.0071 (**n**), ***p = 0.0007(**j**), ***p = 0.0008 (**l**), unpaired two-tailed t-test. **s.** Effect of SD-36 on tumor growth in *Batf3*$^{-/-}$ mice. *Batf3*$^{-/-}$ mice were inoculated with LLC cells and with SD-36 (n = 8) or vehicle (n = 11). Tumor volumes were monitored. **t.** Effect of SD-36 on STAT3 protein in DCs and LLC tumor cells. Immune blotting shows the levels of STAT3 in DCs and LLC tumor cells treated with SD-36 for 12 h, and the ratio of STAT3 to actin expression. **u.** DCs and LLC tumor cells were treated with 1 μM SD-36 for 12 h. Intracellular SD-36 was quantified by LC-MS/MS. mean ± SEM, n = 4, **p = 0.0011, unpaired two-tailed t-test. **v.** Role of SD-36 in DCs. MC38 tumor-bearing mice were treated with SD-36 or vehicle. Immune blotting shows key transcriptional factors in DCs isolated from spleens. One of three experiments is shown. **w.** Effect of cDC1 STAT3 in SD-36-regulated tumor progression. MC38 tumor bearing *Stat3*$^{+/+}$ and *Stat3*$^{-/-}$ mice were treated with SD-36 or vehicle. Tumor volume was determined. mean ± SEM, n = 7, **p = 0.0056, two-way ANOVA. **x.** Role of cDC1 STAT3 in SD-36-regulated anti-tumor immunity. *Stat3*$^{+/+}$ and *Stat3*$^{-/-}$ cDC1s were transferred into MC38-bearing *Batf3*$^{-/-}$ mice. These mice were treated with SD-36. Tumor volume was monitored. mean ± SEM, n = 5, **p = 0.002, two-way ANOVA. Source data contained unprocessed WB.

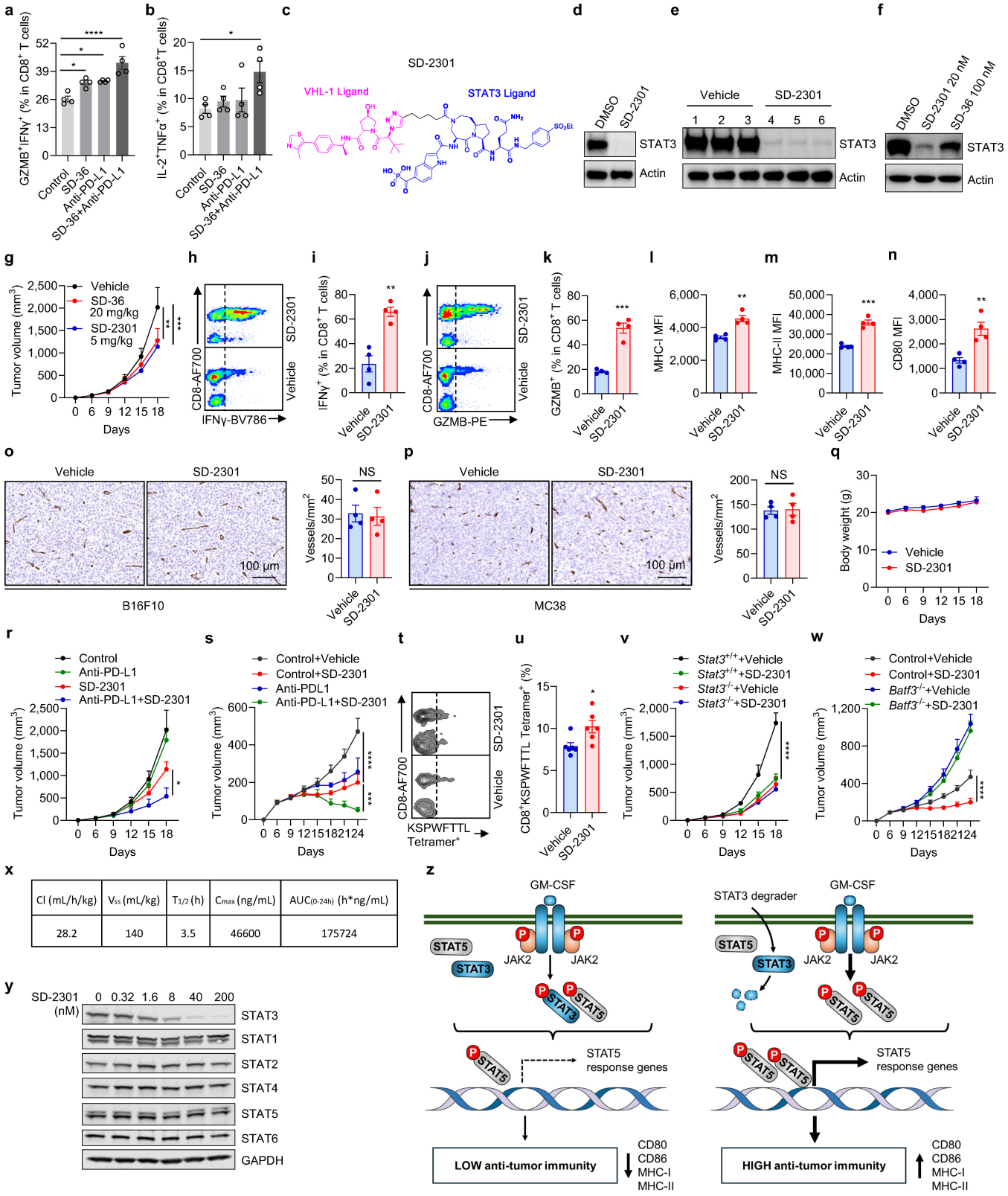

Extended Data Fig. 6 | See next page for caption.

Extended Data Fig. 6 | STAT3 degradation synergizes ICB. a-b. Effect of SD-36 on ICB efficacy in humans in vitro. DCs from human ovarian cancer tissues were pretreated with SD-36, washed, and co-cultured with T cells in the presence of anti-human PD-L1 for 3 days. FACS shows the percentage of $GZMB^+IFN\gamma^+$ (**a**) and $IL\text{-}2^+TNF\alpha^+$ (**b**) $CD8^+$ T cells, mean ± SEM, n = 4, $^*p = 0.0237$ (**a**, control vs. SD-36), $^*p = 0.0135$ (**a**, control vs. Anti-PD-L1), $^*p = 0.0302$ (**b**), $^{****}p < 0.0001$ (**a**), one-way ANOVA. **c**. Chemical structure of SD-2301 structure. **d**. Effect of SD-2301 on STAT3 expression in DCs in vitro. DCs were treated with SD-2301 (50 nM) for 24 h. Immune blotting shows STAT3 protein. One of 3 is shown. **e**. Effect of SD-2301 on STAT3 expression in DCs in vivo. Wild type mice bearing peritoneal B16F10 tumors were treated SD-2301 (5 mg/kg). Immune blotting shows STAT3 expression in peritoneal DCs. n = 3/group. **f**. Comparison of the effect of SD-2301 and SD-36 on STAT3 degradation in mouse DCs. DCs were treated with SD-2301 and SD-36 for 24 h. Immune blotting shows STAT3 expression in DCs. One of three experiments is shown. **g-n**. Comparison of the anti-tumor effect of SD-2301 and SD-36. B16F10 bearing mice were treated with SD-2301 (5 mg/kg) or SD-36 (20 mg/kg) every 3 days. Tumor volume was monitored (**g**). FACS shows the expression of IFNγ (**h**, **i**) and GZMB (**j**, **k**) in B16F10 infiltrating $CD8^+$ T cells, and the expression of MHC-I (**l**), MHC-II (**m**), and CD80 (**n**) in tumor infiltrating cDC1s. MFI, mean fluorescence intensity. means ± SEM, n = 7 (**g**), n = 4 (**i**, **k**, **l**, **m**, **n**), $^{**}p = 0.0023$ (**g**), $^{***}p = 0.0003$ (**g**), two-way ANOVA (**g**); $^{**}p = 0.0014$ (**i**), $^{**}p = 0.0015$ (**l**), $^{**}p = 0.0046$ (**n**), $^{***}p = 0.0001$ (**k**), $^{***}p = 0.0001$ (**m**), unpaired two-tailed t-test (**i**, **k**, **l**, **m**, **n**). **o-p**. Effect of SD-2301 on blood vessels in tumors. B16-F10 and MC38 bearing mice were treated with SD-2301. $CD31^+$ vessel density was quantified in B16-F10 (**o**) and MC38 (**p**) tumors. Representative immunohistochemical staining images and the quantification of $CD31^+$ vessel densities are shown. n = 4 tumors, NS, not significant, unpaired two-tailed t-test. **q**. Effect of SD-2301 on mouse body weights. B16F10 bearing mice were treated with SD-2301 (5 mg/kg) every 3 days for 18 days. Mouse body weights were monitored. **r-s**. Effect of SD-2301 on ICB efficacy in vivo. B16F10 (**r**) or MC38 (**s**) bearing mice were treated with SD-2301, anti-PD-L1, and their combination. The group of B16F10 bearing mice (**r**) treated with SD-2301 is identical to that shown in Extended Data Fig. 6g. Tumor volumes were monitored. mean ± SEM, n = 7, $^*p = 0.0106$, $^{***}p = 0.0009$, $^{****}p < 0.0001$, two-way ANOVA. **t-u**. Effect of SD-2301 on neoantigen specific $CD8^+$ T cell response. MC38 bearing mice were treated with SD-2301 or vehicle. FACS shows the percentage of tumor infiltrating KSPWFTTL $tetramer^+CD8^+$ T cells. means ± SEM, n = 6, $^*p = 0.0216$, unpaired two-tailed t-test. **v**. Effect of SD-2301 on the role of STAT3 in DC-regulated tumor progression. B16F10 tumor bearing $Stat3^{+/+}$ and $Stat3^{-/-}$ mice were treated with SD-2301 or vehicle. Tumor volumes were monitored. mean ± SEM, n = 7, $^{****}p < 0.0001$, Two-way ANOVA. **w**. Effect of SD-2301 on cDC1-regulated tumor progression. MC38 bearing $Batf3^{+/+}$ and $Batf3^{-/-}$ mice were treated with SD-2301 or vehicle. The group of control mice treated with SD-2301 is identical to that shown in Extended Data Fig. 6s. Tumor volumes were monitored. mean ± SEM, n = 7, $^{****}p < 0.0001$, Two-way ANOVA. **x**. Pharmacokinetics (PK) of SD-2301 in mice. Female CD-1 mice (n = 3) were administered with SD-2301 (5 mg/kg). Blood samples were collected for PK analysis. Cl, clearance; Vss, volume of distribution at steady state; $T_{1/2}$, elimination half-life; C_{max}, maximum drug concentration; AUC, area-under-the-curve. **y**. Effect of SD-2301 on STAT3 expression in human immune cells. Human peripheral blood mononuclear cells were treated with different concentrations of SD-2301 for 14 h. The immunoblots show the expression levels of STATs. One of two repeats. **z**. The schematic diagram shows that STAT3 restrains the JAK2-STAT5 signaling pathway, thereby reducing STAT5-dependent DC maturation and lessening T cell immunity and immunotherapy effectiveness. Source data contained unprocessed WB.

Extended Data Table 1 | Clinical characteristics and RNA sequencing analysis of patient cohort 1

	Patient no.	HR	95% CI	p-value	Significance
Age					
Below Median	46 (50%)	ref	ref	ref	
Above Median	46 (50%)	0.982	(0.595, 1.624)	0.945	*ns*
Median and Range	64.8, (23.5-94.6)				
Immunotherapy					
anti-PD1/anti-PDL1	89 (96.7%)	ref	ref	ref	
anti-CTLA4 + anti-PD1/L1	3 (3.3%)	0.455	(0.101, 2.051)	0.305	*ns*
STAT ratio + DC1 maturation					
STAT5/STAT3 High DC1 Low	14 (15.2%)	ref	ref	ref	
STAT5/STAT3 High DC1 High	32 (30.4%)	0.457	(0.210, 0.998)	0.049	*
STAT5/STAT3 Low DC1 High	14 (15.2%)	0.697	(0.286, 1.698)	0.428	*ns*
STAT5/STAT3 Low DC1 Low	32 (30.4%)	0.693	(0.332, 1.446)	0.329	*ns*
Metastatic Sites					
LN					
no	43 (46.7%)	ref	ref	ref	
yes	49 (53.3%)	0.626	(0.378, 1.038)	0.069	*ns*
Bone					
no	71 (77.2%)	ref	ref	ref	
yes	21 (22.8%)	1.628	(0.903, 2.933)	0.105	*ns*
Lung					
yes	38 (41.3%)	-	-	-	
no	54 (58.7%)	-	-	-	
Liver					
yes	17 (18.5%)	-	-	-	
no	75 (81.5%)	-	-	-	
Sex					
Male	48 (52.2%)	-	-	-	
Female	44 (47.8%)	-	-	-	
Race					
Caucasian	86 (93.5%)	-	-	-	
African American	3 (3.3%)	-	-	-	
Asian	1 (1.1%)	-	-	-	
Hispanic	1 (1.1%)	-	-	-	
Middle Eastern	1 (1.1%)	-	-	-	
Cancer Type					
Melanoma	8 (8.7%)	-	-	-	
Bladder	14 (15.2%)	-	-	-	
Breast	11 (12%)	-	-	-	
GI	3 (3.3%)	-	-	-	
HN	23 (25%)	-	-	-	
Kidney	5 (5.4%)	-	-	-	
Lung	5 (5.4%)	-	-	-	
Lymphoma	3 (3.3%)	-	-	-	
Prostate	9 (10%)	-	-	-	
Sarcoma	6 (6.5%)	-	-	-	
Other	5 (5.4%)	-	-	-	

Pre-treatment tumor biopsies from these patients underwent bulk RNA sequencing analysis. It includes patient age, the types of ICB treatments, STAT ratio + DC1 maturation, metastatic sites, cancer types. n=92, *p=0.049. A Cox proportional hazards model was used (two-sided test) to analyze overall survival, with covariates including DC1 maturation and *STAT5*/*STAT3* ratio stratification, presence of bone metastasis, lymph node metastasis, median age, and ICB target. LN, lymph node; GI, gastrointestinal; HN, head & neck.

Extended Data Table 2 | Clinical characteristics and RNA sequencing analysis of patient cohort 2

	Gide et al. Cohort	Van Allen et al. Cohort
Age at Immunotherapy (Average)	61.7	59.9
Below Mean	35 (48.6%)	19 (45.2%)
Above Mean	37 (51.4%)	23 (54.8%)
Range	24-90	22-83
Median	62	61
Sex		
Male	47 (65.3%)	28 (66.7%)
Female	25 (34.7%)	14 (33.3%)
Site of Biopsy		
SQ	46 (63.9%)	37 (88.1%)
LN	19 (26.4%)	NA
Lung	3 (4.2%)	NA
Liver	NA	NA
Mucosa	2 (2.8%)	2 (4.8%)
Abdomen	1 (1.4%)	NA
Brain	1 (1.4%)	NA
Bowel	NA	NA
Occult	NA	3 (7.1%)
Histology		
Nodular	NA	11 (26.2%)
Superficial Spreading	NA	11 (26.2%)
Unknown or NA	NA	16 (38.1%)
Acral Lentiginous	NA	4 (9.5%)
Treatment		
anti-CTLA4 + anti-PD1	31 (43.1%)	NA
anti-PD1	41 (56.9%)	NA
anti-CTLA4	NA	42 (100%)
Prior Lines of Therapy		
0	NA	9 (21.4%)
1+	NA	33 (78.6%)
Disease Stage		
M0	NA	1 (2.4%)
M1a	NA	3 (7.1%)
M1b	NA	7 (16.7%)
M1c	NA	31 (73.8%)
M1d	NA	0 (0%)
RECIST Response		
CR	13 (18.1%)	2 (4.8%)
PR	26 (36.1%)	5 (11.9%)
SD	11 (15.3%)	7 (16.7%)
PD	22 (30.5%)	27 (64.3%)
NA	NA	1 (2.4%)

The table provides clinical, pathological, anatomic, and therapeutic information on melanoma patients treated with ICB. CR, complete response; PR, partial response; SD, stable disease (SD); PD, progressive disease (PD); NA, Undermined. SQ, subcutaneous; LN, lymph node.

Extended Data Table 3 | Primer sequences for Real-Time PCR

Primer ID	Primer Sequences (5'-3')
Mouse *Gmrα* qPCR Primer Forward	CAGTTTGAGGTCCAGTGGCAGA
Mouse *Gmrα* qPCR Primer Reverse	CCAGTGCTTCATCCTCGTGTCG
Mouse *Gmrβ* qPCR Primer Forward	GCAGGCTTCTTGCTGAGCAACA
Mouse *Gmrβ* qPCR Primer Reverse	GGAAGTTGCTCTGTGGATTCGG
Mouse *Il2ra* qPCR Primer Forward	GCGTTGCTTAGGAAACTCCTGG
Mouse *Il2ra* qPCR Primer Reverse	GCATAGACTGTGTTGGCTTCTGC
Mouse *Il2rb* qPCR Primer Forward	CTCAAGTGCCACATCCCAGATC
Mouse *Il2rb* qPCR Primer Reverse	AGCACTTCCAGCGGAGAGATCT
Mouse *Il2rg* qPCR Primer Forward	GGAGCAACAGAGATCGAAGCTG
Mouse *Il2rg* qPCR Primer Reverse	CCACAGATTGGGTTATAGCGGC
Mouse *Il3ra* qPCR Primer Forward	GAGGTTTACCCTCGGAAGCTCA
Mouse *Il3ra* qPCR Primer Reverse	AGCACCGTAGCCACTGAAGTCA
Mouse *Il5ra* qPCR Primer Forward	AGGGTTTGAGCAGCTTGCTGTG
Mouse *Il5ra* qPCR Primer Reverse	CCACTGTGACATTCCTTGGAGG
Mouse *Il7r* qPCR Primer Forward	CACAGCCAGTTGGAAGTGGATG
Mouse *Il7r* qPCR Primer Reverse	GGCATTTCACTCGTAAAAGAGCC
Mouse *Il15ra* qPCR Primer Forward	GACACCAAAGGTGACCTCACAG
Mouse *Il15ra* qPCR Primer Reverse	CTGTCTCTGTGGTCATTGCGGT
Mouse *Il21r* qPCR Primer Forward	CACTGACTACCTCTGGACCATC
Mouse *Il21r* qPCR Primer Reverse	GCAGAAGGTCTCTTGGTCCTGA
Mouse *Actb* qPCR Primer Forward	AGATCAAGATCATTGCTCCTCCT
Mouse *Actb* qPCR Primer Reverse	ACGCAGCTCAGTAACAGTCC
Mouse *H2-D1* Promoter qPCR Primer Forward	CTCCACTGCATCCCTAAGCG
Mouse *H2-D1* Promoter qPCR Primer Reverse	ACAAGCCCGACTCACTGTTT
Mouse *H2-Eb1* Promoter qPCR Primer Forward	AGTTTCAGAAGGGGACCTGC
Mouse *H2-Eb1* Promoter qPCR Primer Reverse	ACTGCTTTGCCACTGGATTG
Mouse *Cd80* Promoter qPCR Primer Forward	TCCCTGGACGCTTCCATTTC
Mouse *Cd80* Promoter qPCR Primer Reverse	TGTGTAAGCTGTCCTGGCTG
Mouse *Cd86* Promoter qPCR Primer Forward	CCCTCAAGACTGAAACCGAAC
Mouse *Cd86* Promoter qPCR Primer Reverse	ACTGTGTACCCTGGTGGTTG

nature portfolio

Corresponding author(s): Weiping Zou, Shaomeng Wang

Last updated by author(s): 03/05/2025

Reporting Summary

Nature Portfolio wishes to improve the reproducibility of the work that we publish. This form provides structure for consistency and transparency in reporting. For further information on Nature Portfolio policies, see our Editorial Policies and the Editorial Policy Checklist.

Statistics

For all statistical analyses, confirm that the following items are present in the figure legend, table legend, main text, or Methods section.

n/a	Confirmed
☐	☒ The exact sample size (*n*) for each experimental group/condition, given as a discrete number and unit of measurement
☐	☒ A statement on whether measurements were taken from distinct samples or whether the same sample was measured repeatedly
☐	☒ The statistical test(s) used AND whether they are one- or two-sided *Only common tests should be described solely by name; describe more complex techniques in the Methods section.*
☐	☒ A description of all covariates tested
☐	☒ A description of any assumptions or corrections, such as tests of normality and adjustment for multiple comparisons
☐	☒ A full description of the statistical parameters including central tendency (e.g. means) or other basic estimates (e.g. regression coefficient) AND variation (e.g. standard deviation) or associated estimates of uncertainty (e.g. confidence intervals)
☐	☒ For null hypothesis testing, the test statistic (e.g. *F*, *t*, *r*) with confidence intervals, effect sizes, degrees of freedom and *P* value noted *Give P values as exact values whenever suitable.*
☒	☐ For Bayesian analysis, information on the choice of priors and Markov chain Monte Carlo settings
☒	☐ For hierarchical and complex designs, identification of the appropriate level for tests and full reporting of outcomes
☐	☒ Estimates of effect sizes (e.g. Cohen's *d*, Pearson's *r*), indicating how they were calculated

Our web collection on statistics for biologists contains articles on many of the points above.

Software and code

Policy information about availability of computer code

Data collection	The samples for flow cytometry were collected on a FACS LSR Fortessa (BD Biosciences). In vivo bioluminescence signal was assessed with the IVIS Spectrum In Vivo Imaging System (PerkinElmer). Immunoblotting images were obtained using X-ray Film, LI-COR Odessey CLx (LI-COR Biosciences) and ChemiDoc Imaging System (Bio-Rad). Immunohistochemistry (IHC) was performed by the University of Michigan Pathology Core.
Data analysis	FACS data were analyzed with FACSDiva 9.0 (BD Biosciences). Western Blotting data were processed and analyzed by Image Lab 6.1 (BIO-RAD), and Image J 1.51n (NIH). IHC data were analyzed by QuPath 0.5.1. Statistical analysis and data presentation were performed by R packages, and Graphpad Prism 10.2.2.

For manuscripts utilizing custom algorithms or software that are central to the research but not yet described in published literature, software must be made available to editors and reviewers. We strongly encourage code deposition in a community repository (e.g. GitHub). See the Nature Portfolio guidelines for submitting code & software for further information.

Data

Policy information about availability of data

All manuscripts must include a data availability statement. This statement should provide the following information, where applicable:

- Accession codes, unique identifiers, or web links for publicly available datasets
- A description of any restrictions on data availability
- For clinical datasets or third party data, please ensure that the statement adheres to our policy

Clinical sequencing data are publicly available with raw data available upon request from dbGaP phs000673.v5.p1.
RNA-seq data newly generated in this study for in vitro analysis have been deposited in the GEO repository at NCBI under accession GSE289764.
Single-cell RNA sequencing data that support the findings of this study was downloaded from Gene Expression Omnibus (GEO) under the accession number GSE169246.
The two original melanoma RNA-seq datasets were deposited in the European Nucleotide Archive (ENA) under accession number PRJEB23709 and in dbGaP under accession number phs000452.v2.p1. The processed data for these two melanoma datasets can be found at https://ngdc.cncb.ac.cn/icb/resources.
The remaining data are available within the Article, Supplementary Information or Source Data file. Source data are provided with this paper.

Research involving human participants, their data, or biological material

Policy information about studies with human participants or human data. See also policy information about sex, gender (identity/presentation), and sexual orientation and race, ethnicity and racism.

Reporting on sex and gender	The biological sex of all patients undergoing ICB therapy was documented.
Reporting on race, ethnicity, or other socially relevant groupings	The race and cancer type of all patients who underwent ICB therapy can be found in Extended data Table 1.
Population characteristics	The relevant characteristics of all patients who underwent ICB therapy can be found in Extended data Table 1.
Recruitment	Patients who underwent ICB therapy were recruited from the University of Michigan Hospital in Ann Arbor, MI, USA. No potential self-selection biases were identified.
Ethics oversight	All human studies were conducted under the oversight and approval of the Institutional Review Board at the School of Medicine, University of Michigan.

Note that full information on the approval of the study protocol must also be provided in the manuscript.

Field-specific reporting

Please select the one below that is the best fit for your research. If you are not sure, read the appropriate sections before making your selection.

☒ Life sciences ☐ Behavioural & social sciences ☐ Ecological, evolutionary & environmental sciences

For a reference copy of the document with all sections, see nature.com/documents/nr-reporting-summary-flat.pdf

Life sciences study design

All studies must disclose on these points even when the disclosure is negative.

Sample size	No sample size calculation were performed. For in vivo studies, 5-11 mice per group are sufficient to detect meaningful biological differences with good reproducibility. For in vitro studies, all the experiments were replicated at least for 2 individual, independent experiments. Group sizes of experiments were selected empirically based upon previous published literatures and prior knowledge (Wang et al, 2019; Yu et al, 2021; Zhou et al, 2021). All samples sizes for various assays are listed in the Methods section or the figure legends. References: Wang, W. et al. CD8+ T cells regulate tumour ferroptosis during cancer immunotherapy. Nature 569, 270–274 (2019). Yu, J. et al. Liver metastasis restrains immunotherapy efficacy via macrophage-mediated T cell elimination. Nat Med 27, 152–164 (2021). Zhou, J. et al. The ubiquitin ligase MDM2 sustains STAT5 stability to control T cell-mediated antitumor immunity. Nat Immunol 22, 460-470 (2021).
Data exclusions	No data were excluded from the manuscript.
Replication	As reported in the figure legends, the findings were reliably reproduced.
Randomization	For all in vivo experiments, animals were randomly assigned into a treatment group after tumor inoculation. The starting tumor burden in the treatment and control groups were similar before treatment. All groups were age and sex matched. In experiments not involving mice, we did not randomize because in vitro studies were observational and replicated at least for 2 independent experiment.

Blinding

Experiments were not performed in a blinded manner. The investigator needed to know the treatment groups in order to perform the study. Blinding was not possible as most of the data acquisition and analysis were done by a single person. Blinding would have required at least two individuals for each experiment which was not feasible during the course of the study. The data were observational, not at risk of bias in interpretation. All data were acquired and analyzed by software with objective standard, thus blinding was not relevant to the study.

Reporting for specific materials, systems and methods

We require information from authors about some types of materials, experimental systems and methods used in many studies. Here, indicate whether each material, system or method listed is relevant to your study. If you are not sure if a list item applies to your research, read the appropriate section before selecting a response.

Materials & experimental systems

n/a	Involved in the study
☐	☒ Antibodies
☐	☒ Eukaryotic cell lines
☒	☐ Palaeontology and archaeology
☐	☒ Animals and other organisms
☒	☐ Clinical data
☒	☐ Dual use research of concern
☒	☐ Plants

Methods

n/a	Involved in the study
☒	☐ ChIP-seq
☐	☒ Flow cytometry
☒	☐ MRI-based neuroimaging

Antibodies

Antibodies used

For Western blots, primary antibodies were used at a dilution of 1:1000 unless otherwise specified.
anti-STAT1 (D1K9Y, #14994), anti-STAT2 (D9J7L, #72604), anti-STAT3 (Rabbit, 79D7, #4904; Mouse, 124H6, #9139), anti-STAT4 (C46B10, #2653), anti-STAT5 (D2O6Y, #94205), anti-STAT6 (D3H4, #5397), anti-JAK1 (6G4, #3344), anti-JAK2 (D2E12, #3230), anti-JAK3 (D7B12, #8863), anti-TYK2 (E9H4T, #35615), anti-p65 (D14E12, #8242), anti-CD80 (E6J6N, #54521), anti-CD86 (E5W6H, #19589), anti-IL-6Rα (E7H4J, #39837, Lot 1) , anti-GP130 (#3732, Lot 6), anti-pSTAT1 (58D6, #9167), anti-pSTAT3 (D3A7, #9145), anti-pSTAT5 (D47E7, #4322), anti-pSTAT6 (D8S9Y, #56554), anti-pJAK1 (D7N4Z, #74129), anti-pJAK2 (C80C3, #3776), anti-pJAK3 (D44E3, #5031), anti-pp65 (93H1, #3033), anti-β-actin (#4967) were from Cell Signaling Technology. Anti-JAK2 (C-10, sc-390539), Anti-GMRβ (F-12, sc-393281), anti-β-actin (C4, sc-47778) were from Santa Cruz Biotechnology. Anti-pTYK2 (PA5-37762) was from Invitrogen. For secondary antibodies, HRP horse anti-mouse IgG antibody (PI-2000, 1:5000), HRP goat anti-rabbit IgG (PI-1000, 1:5000) were from Vector Laboratories.
For IHC, Anti-CD31 (D8V9E, #77699, Lot 6, 1:100) was from Cell Signaling Technology.
For Flow cytometry, antibodies were used at a dilution of 1:50 unless otherwise specified.
PE-CY7 Anti-Mouse CD11c (clone HL3, #558079, Lot 3334101),FITC Anti-mouse-CD90 (clone 30-H12, #553013, Lot 4176004), FITC anti-mouse CD3 (clone 17A2, #561798, Lot 1286349), FITC anti-mouse CD45R/B220 (clone RA3-6B2, #553088, Lot 3110705), PE anti-mouse CD80 (Clone 16-10A1, 553769, Lot 3298935), BV650 anti-mouse CD80 (Clone 16-10A1, 563687, Lot 0015825), APC-R700 anti-mouse CD8 (clone 53-6.7, #564983, Lot 4249800), V500 anti-mouse CD8 (clone 53-6.7, #560776, Lot 1116792), PerCP anti-mouse CD45 (clone 30-F11, #557235, Lot 8179968), APC-CY7 anti-mouse CD4 (clone GK1.5, #552051, Lot 4144628), BV786 anti-mouse-IFNγ (clone XMG1.2, #563773, Lot 4008777), APC anti-mouse CD4 (clone RM4.5, #553051, Lot 0231898), BV605 anti-mouse H-2 class I (clone M1/42, #749709), PE anti-granzyme B (clone GB11, #561142, Lot 4149375), APC anti-mouse-IL-2 (clone JES6-5H4, #554429, Lot 3242915), Alexa Fluor 700 Mouse anti-Ki-67 (Clone B56, #561277, Lot 1154059), PE-CY7 Anti-mouse-TNFα (clone MP6-XT22, #557644, Lot 4256222), APC-Cy7 Anti-mouse-CD90 (clone 53-2.1, # 561641), FITC Anti-Human IFN-γ (Clone B27, #554700, Lot 2283301), PE-Cy7 Anti-Human TNF (Clone MAb11, #557647, Lot 8143874), R718 Anti-Human CD8 (Clone RPA-T8, #567056) were purchased from BD Biosciences. BV421 anti-mouse I-A/I-E (Clone M5/114.15.2, #404-5321-82, Lot 3037246), PE anti-mouse CD86 (Clone GL1, #12-0862-82, Lot 2863198), APC anti-mouse MHC class I (clone AF6-88.5.5.3, #17-5958-82, Lot 2961236), Pacific Orange anti-mouse CD45 (clone HI30, #MHCD4530, Lot 2668640), PE-Cyanine7 phospho-STAT5 (clone SRBCZX, #25-9010-42, Lot 2442266, 1:20) were purchased from Thermo Fisher Scientific. PE Anti- Phospho-STAT3 (clone 13A3-1, #651004, Lot B341628, 1:20), APC/Cyanine7 anti-mouse XCR1 (clone ZET, #148224, Lot B388581) were purchased from BioLegend.

Validation

All antibodies used were commercial and validated for the appropriate application.
anti-STAT1 (D1K9Y, #14994, Lot 8)
https://www.cellsignal.com/products/primary-antibodies/stat1-d1k9y-rabbit-mab/14994
anti-STAT2 (D9J7L, #72604, Lot 2)
https://www.cellsignal.com/products/primary-antibodies/stat2-d9j7l-rabbit-mab/72604
anti-STAT3 (Rabbit, 79D7, #4904, Lot7) https://www.cellsignal.com/products/primary-antibodies/stat3-79d7-rabbit-mab/4904
anti-STAT3 (mouse, 124H6, #9139, Lot 16) https://www.cellsignal.com/products/primary-antibodies/stat3-124h6-mouse-mab/9139
anti-STAT4 (C46B10, #2653, Lot 4)
https://www.cellsignal.com/products/primary-antibodies/stat4-c46b10-rabbit-mab/2653
anti-STAT5 (D2O6Y, #94205, Lot 5)
https://www.cellsignal.com/products/primary-antibodies/stat5-d2o6y-rabbit-mab/94205
anti-STAT6 (D3H4, #5397, Lot 5)
https://www.cellsignal.com/products/primary-antibodies/stat6-d3h4-rabbit-mab/5397
anti-JAK1 (6G4, #3344, Lot 6)

https://www.cellsignal.com/products/primary-antibodies/jak1-6g4-rabbit-mab/3344
anti-JAK2 (D2E12, #3230, Lot 13)
https://www.cellsignal.com/products/primary-antibodies/jak2-d2e12-xp-rabbit-mab/3230
anti-JAK3 (D7B12, #8863, Lot 3)
https://www.cellsignal.com/products/primary-antibodies/jak3-d7b12-rabbit-mab/8863
anti-TYK2 (E9H4T, #35615, Lot 1)
https://www.cellsignal.com/products/primary-antibodies/tyk2-e9h4t-rabbit-mab/35615
anti-p65 (D14E12, #8242, Lot 16)
https://www.cellsignal.com/products/primary-antibodies/nf-kb-p65-d14e12-xp-rabbit-mab/8242
anti-CD80 (E6J6N, #54521, Lot 1)
https://www.cellsignal.com/products/primary-antibodies/cd80-e6j6n-rabbit-mab/54521
anti-CD86 (E5W6H, #19589, Lot 5)
https://www.cellsignal.com/products/primary-antibodies/cd86-e5w6h-rabbit-mab/19589
anti-IL-6Rα (E7H4J, #39837, Lot 1)
https://www.cellsignal.com/products/primary-antibodies/il-6ra-cd126-e7h4j-rabbit-mab/39837
anti-GP130 (#3732, Lot 6)
https://www.cellsignal.com/products/primary-antibodies/gp130-antibody/3732
anti-pSTAT1 (58D6, #9167, Lot 18)
https://www.cellsignal.com/products/primary-antibodies/phospho-stat1-tyr701-58d6-rabbit-mab/9167
anti-pSTAT3 (D3A7, #9145, Lot 43)
https://www.cellsignal.com/products/primary-antibodies/phospho-stat3-tyr705-d3a7-xp-rabbit-mab/9145
anti-pSTAT5 (D47E7, #4322, Lot 5)
https://www.cellsignal.com/products/primary-antibodies/phospho-stat5-tyr694-d47e7-xp-rabbit-mab/4322
anti-pSTAT6 (D8S9Y, #56554, Lot 1)
https://www.cellsignal.com/products/primary-antibodies/phospho-stat6-tyr641-d8s9y-rabbit-mab/56554
anti-pJAK1 (D7N4Z, #74129, Lot 2)
https://www.cellsignal.com/products/primary-antibodies/phospho-jak1-tyr1034-1035-d7n4z-rabbit-mab/74129
anti-pJAK2 (C80C3, #3776, Lot 13)
https://www.cellsignal.com/products/primary-antibodies/phospho-jak2-tyr1007-1008-c80c3-rabbit-mab/3776
anti-pJAK3 (D44E3, #5031, Lot 7)
https://www.cellsignal.com/products/primary-antibodies/phospho-jak3-tyr980-981-d44e3-rabbit-mab/5031
anti-pp65 (93H1, #3033, Lot 19)
https://www.cellsignal.com/products/primary-antibodies/phospho-nf-kb-p65-ser536-93h1-rabbit-mab/3033
anti-β-actin (Rabbit, #4967, Lot 15)
https://www.cellsignal.com/products/primary-antibodies/b-actin-antibody/4967
anti-β-actin (Mouse, C4, sc-47778, Lot F1323)
https://www.scbt.com/p/beta-actin-antibody-c4
Anti-JAK2 (C-10, sc-390539, Lot #K0822)
https://www.scbt.com/p/jak2-antibody-c-10
Anti-GMRβ (F-12, sc-393281, Lot #K1921)
https://www.scbt.com/p/il-3-il-5-gm-csfrbeta-antibody-f-12
Anti-pTYK2 (PA5-37762, Lot ZC4271911) https://www.thermofisher.com/antibody/product/Phospho-TYK2-Tyr1054-Antibody-Polyclonal/PA5-37762
HRP horse anti-mouse IgG antibody (PI-2000, Lot ZK040)
https://vectorlabs.com/products/peroxidase-horse-anti-mouse-igg/
HRP goat anti-rabbit IgG (PI-1000, Lot ZK0623), validated by manufacturer and citations at https://vectorlabs.com/products/peroxidase-goat-anti-rabbit-igg/
Anti-CD31 (D8V9E, #77699, Lot 6)
https://www.cellsignal.com/products/primary-antibodies/cd31-pecam-1-d8v9e-xp-rabbit-mab/77699
PE-CY7 Anti-Mouse CD11c (clone HL3, #558079, Lot 3334101),
https://www.bdbiosciences.com/en-eu/products/reagents/flow-cytometry-reagents/research-reagents/single-color-antibodies-ruo/pe-cy-7-hamster-anti-mouse-cd11c.558079?tab=product_details
FITC Anti-mouse-CD90 (clone 30-H12, #553013, Lot 4176004), https://www.bdbiosciences.com/en-eu/products/reagents/flow-cytometry-reagents/research-reagents/single-color-antibodies-ruo/fitc-rat-anti-mouse-cd90-2.553013?tab=product_details
FITC anti-mouse CD3 (clone 17A2, #561798, Lot 1286349), https://www.bdbiosciences.com/en-eu/products/reagents/flow-cytometry-reagents/research-reagents/single-color-antibodies-ruo/fitc-rat-anti-mouse-cd3-molecular-complex.561798?tab=product_details
APC-Cy7 Anti-mouse-CD90 (clone 53-2.1, # 561641), https://www.bdbiosciences.com/en-us/products/reagents/flow-cytometry-reagents/research-reagents/single-color-antibodies-ruo/apc-cy-7-rat-anti-mouse-cd90-2.561641?tab=product_details
FITC anti-mouse CD45R/B220 (clone RA3-6B2, #553088, Lot 3110705),
https://www.bdbiosciences.com/en-eu/products/reagents/microscopy-imaging-reagents/immunofluorescence-reagents/fitc-rat-anti-mouse-cd45r-b220.553088?tab=product_details
PE anti-mouse CD80 (Clone 16-10A1, 553769, Lot 3298935),
https://www.bdbiosciences.com/en-eu/products/reagents/flow-cytometry-reagents/research-reagents/single-color-antibodies-ruo/pe-hamster-anti-mouse-cd80.553769?tab=product_details
BV650 anti-mouse CD80 (Clone 16-10A1, 563687, Lot 0015825),
https://www.bdbiosciences.com/en-eu/products/reagents/flow-cytometry-reagents/research-reagents/single-color-antibodies-ruo/bv650-hamster-anti-mouse-cd80.563687?tab=product_details
APC-R700 anti-mouse CD8 (clone 53-6.7, #564983, Lot 4249800),
https://www.bdbiosciences.com/en-eu/products/reagents/flow-cytometry-reagents/research-reagents/single-color-antibodies-ruo/apc-r700-rat-anti-mouse-cd8a.564983?tab=product_details
V500 anti-mouse CD8 (clone 53-6.7, #560776, Lot 1116792),
https://www.bdbiosciences.com/en-us/products/reagents/flow-cytometry-reagents/research-reagents/single-color-antibodies-ruo/v500-rat-anti-mouse-cd8a.560776?tab=product_details
PerCP anti-mouse CD45 (clone 30-F11, #557235, Lot 8179968),
https://www.bdbiosciences.com/en-us/products/reagents/flow-cytometry-reagents/research-reagents/single-color-antibodies-ruo/

percp-rat-anti-mouse-cd45.557235?tab=product_details
APC-CY7 anti-mouse CD4 (clone GK1.5, #552051, Lot 4144628),
https://www.bdbiosciences.com/en-eu/products/reagents/flow-cytometry-reagents/research-reagents/single-color-antibodies-ruo/apc-cy-7-rat-anti-mouse-cd4.552051?tab=product_details
BV786 anti-mouse-IFNγ (clone XMG1.2, #563773, Lot 4008777), https://www.bdbiosciences.com/en-eu/products/reagents/flow-cytometry-reagents/research-reagents/single-color-antibodies-ruo/bv786-rat-anti-mouse-ifn.563773?tab=product_details
PE anti-granzyme B (clone GB11, #561142, Lot 4149375),
https://www.bdbiosciences.com/en-eu/products/reagents/flow-cytometry-reagents/research-reagents/single-color-antibodies-ruo/pe-mouse-anti-human-granzyme-b.561142?tab=product_details
APC anti-mouse-IL-2 (clone JES6-5H4, #554429, Lot 3242915),
https://www.bdbiosciences.com/en-eu/products/reagents/flow-cytometry-reagents/research-reagents/single-color-antibodies-ruo/apc-rat-anti-mouse-il-2.554429?tab=product_details
PE-CY7 Anti-mouse-TNFα (clone MP6-XT22, #557644, 4256222),
https://www.bdbiosciences.com/en-eu/products/reagents/flow-cytometry-reagents/research-reagents/single-color-antibodies-ruo/pe-cy-7-rat-anti-mouse-tnf.557644?tab=product_details
Brilliant Violet 421 anti-mouse I-A/I-E (Clone M5/114.15.2, #404-5321-82, Lot 3037246), https://www.thermofisher.com/antibody/product/MHC-Class-II-I-A-I-E-Antibody-clone-M5-114-15-2-Monoclonal/404-5321-82
PE anti-mouse CD86 (Clone GL1, #12-0862-82, Lot 2863198)
https://www.thermofisher.com/antibody/product/CD86-B7-2-Antibody-clone-GL1-Monoclonal/12-0862-82
APC anti-mouse MHC class I (H-2Kb) (clone AF6-88.5.5.3, #17-5958-82, Lot 2961236),
https://www.thermofisher.com/antibody/product/MHC-Class-I-H-2Kb-Antibody-clone-AF6-88-5-5-3-Monoclonal/17-5958-82?imageId=91186
Pacific Orange anti-mouse CD45 (clone HI30, #MHCD4530, Lot 2668640),
https://www.thermofisher.com/antibody/product/CD45-Antibody-clone-HI30-Monoclonal/MHCD4530
PE-Cyanine7 phospho-STAT5 monoclonal antibody (clone SRBCZX, #25-9010-42, Lot 2442266)
https://www.thermofisher.com/antibody/product/Phospho-STAT5-Tyr694-Antibody-clone-SRBCZX-Monoclonal/25-9010-42
PE Anti- Phospho-STAT3 (Tyr705) (clone 13A3-1, #651004, Lot B341628)
https://www.biolegend.com/de-de/products/pe-anti-stat3-phospho-tyr705-antibody-12914
APC/Cyanine7 anti-mouse XCR1 (clone ZET, #148224, Lot B388581)
https://www.biolegend.com/de-de/products/apc-cyanine7-anti-mouse-rat-xcr1-antibody-16709
FITC Anti-Human IFN-γ (Clone B27, #554700, Lot 2283301)
https://www.bdbiosciences.com/en-us/products/reagents/flow-cytometry-reagents/research-reagents/single-color-antibodies-ruo/fitc-mouse-anti-human-ifn.554700?tab=product_details
PE-Cy7 Anti-Human TNF (Clone MAb11, #557647, Lot 8143874)
https://www.bdbiosciences.com/en-us/products/reagents/flow-cytometry-reagents/research-reagents/single-color-antibodies-ruo/pe-cy-7-mouse-anti-human-tnf.557647?tab=product_details
R718 Anti-Human CD8 (Clone RPA-T8, #567056)
https://www.bdbiosciences.com/en-us/products/reagents/flow-cytometry-reagents/research-reagents/single-color-antibodies-ruo/r718-mouse-anti-human-cd8.567056?tab=product_details
APC anti-mouse CD4 (clone RM4.5, #553051, Lot 0231898)
https://www.bdbiosciences.com/en-us/products/reagents/flow-cytometry-reagents/research-reagents/single-color-antibodies-ruo/apc-rat-anti-mouse-cd4.553051?tab=product_details
BV605 anti-mouse H-2 class I (clone M1/42, #749709),
https://www.bdbiosciences.com/en-us/products/reagents/flow-cytometry-reagents/research-reagents/single-color-antibodies-ruo/bv605-rat-anti-mouse-h-2-class-i.749709?tab=product_details
Alexa Fluor 700 Mouse anti-Ki-67 (Clone B56, #561277, Lot 1154059),
https://www.bdbiosciences.com/en-us/products/reagents/flow-cytometry-reagents/research-reagents/single-color-antibodies-ruo/alexa-fluor-700-mouse-anti-ki-67.561277?tab=product_details

Eukaryotic cell lines

Policy information about cell lines and Sex and Gender in Research

Cell line source(s)	JAWSII, 293T, B16F10, CT26, LLC, EMT-6, and 4T1 were purchased from the American Type Culture Collection (ATCC). MC38 was obtained from the University of Texas Southwestern Medical Center (Dr. Yang-Xin Fu). Ovarian cancer cell line luciferase-ID8 was cited.
Authentication	Cell lines were not authenticated.
Mycoplasma contamination	All cell lines in our laboratory are routinely tested for mycoplasma contamination and cells used in this study are negative for mycoplasma.
Commonly misidentified lines (See ICLAC register)	No misidentified cell lines were used in this study

Animals and other research organisms

Policy information about studies involving animals; ARRIVE guidelines recommended for reporting animal research, and Sex and Gender in Research

Laboratory animals	All mice were maintained under specific pathogen-free housing (~22°C with ~40% humidity) on a 12-hour dark/12-hour light cycle. The following mice (at 6-8 week of age) (The Jackson laboratory) were used for this study: C57BL/6J, BALB/cJ, NOD-scid IL2Rγ null

(NSG), Rag1tm1Mom (Rag1–/–), C57BL/6-Tg(TcraTcrb)1100Mjb/J (OT-I), B6.129S(C)-Batf3tm1Kmm/J (Batf3-/-), B6.129S(Cg)-Stat1tm1Dlv/J (Stat1-/-), B6(129S4)-Xcr1tm1.1(cre) Kmm/J (Xcr1-Cre), B6.129S1-Stat3tm1Xyfu/J (Stat3flox/flox) mice, CD-1 mice were obtained from Charles River Laboratories. Stat5b–/– C57BL/6J mice were from the National Institutes of Health (Warren J. Leonard). Stat3flox/flox mice were crossed with Xcr1-Cre mice to obtain specific STAT3 deficiency in DC1s (Stat3-/- mice). In-house littermates were used in the control arm when specific mouse strains were generated in-house.

Wild animals	The study did not involve wild animals.
Reporting on sex	No specific gender.
Field-collected samples	The study did not involve samples collected from field.
Ethics oversight	All mouse experiments were performed in accordance with protocol approved by the University of Michigan animal care and Use Committee.

Note that full information on the approval of the study protocol must also be provided in the manuscript.

Flow Cytometry

Plots

Confirm that:

☒ The axis labels state the marker and fluorochrome used (e.g. CD4-FITC).

☒ The axis scales are clearly visible. Include numbers along axes only for bottom left plot of group (a 'group' is an analysis of identical markers).

☒ All plots are contour plots with outliers or pseudocolor plots.

☒ A numerical value for number of cells or percentage (with statistics) is provided.

Methodology

Sample preparation	Single-cell suspensions were prepared from fresh mouse tumor tissues or spleen, and lymphocytes were enriched by density gradient centrifugation. For intracellular cytokine staining, lymphocytes were incubated in culture medium containing PMA (phorbol 12-myristate-13-acetate, 5 ng/mL, Sigma Aldrich), Ionomycin (500 ng/mL, Sigma Aldrich), Brefeldin A (1: 1000, BD Biosciences). and Monensin (1: 1000, BD Biosciences) at 37°C for 4 hours. Antibodies were added for 20 minutes for surface staining. The cells were then washed and resuspended in 1 mL of freshly prepared Fix/Perm solution (BD Biosciences) at 4°C for overnight. After being washed with Perm/Wash buffer (BD Biosciences), the cells were stained with antibodies against intracellular proteins for 30 minutes, washed, and fixed in 4% formaldehyde (Sigma Aldrich). For DC1 function detection, lymphocytes were stained with antibodies for 20 minutes at room temperature in the dark, and then cells were analyzed by flow cytometry. For phosphor-protein detection, the cells were initially stained with antibodies for surface staining. After staining, the cells were then washed and resuspended in IC Fixation Buffer (BD Biosciences) for 30 minutes. The samples were centrifuged at 600 x g for 5 minutes at room temperature, discard the supernatant. Resuspended the cell pellet in residual volume and added 1 mL of ice-cold 90-100% methanol. Vortexed to mix and incubated for 30 minutes at 4°C. After being washed with staining buffer, the cells were stained with antibodies against phospho-proteins for 30 minutes, washed, and fixed in 4% formaldehyde (Sigma Aldrich).
Instrument	All samples were read on an BD LSRFortessa cytometer (BD Biosciences).
Software	All data were analyzed with FACS DIVA software v. 9.0 (BD Biosciences).
Cell population abundance	When cells were sorted or enriched, the purity was confirmed by flow cytometry and in each case was above 90% purity.
Gating strategy	The cells were gated based on FSC-A/SSC-A in regions known to contain lymphoid cells and tumor cells. For T cell functional analysis, CD90+CD3+ cells were selected, followed by gating for CD8+ and CD4+ populations. Subsequently, the percentages of IFNγ, granzyme B, IL-2, Ki67, and TNFα cells were analyzed within the CD8+ gate. For dendritic cell (DC) functional analysis, the CD45+ population was initially gated. The CD90+CD3+CD45R+ population was excluded, and then the XCR1+ and CD11c+ populations were gated. Subsequently, the mean fluorescence intensity (MFI) of MHC-I, MHC-II, CD80, and CD86 was analyzed within the CD11c+XCR1+ gate.

☒ Tick this box to confirm that a figure exemplifying the gating strategy is provided in the Supplementary Information.